ISSN: 3023 -8951

CHAOS AND FRACTALS

VOLUME 2, ISSUE 2, JULY 2025

AN INTERDISCIPLINARY JOURNAL OF
NONLINEAR SCIENCE

ADBA

https://journals.adbascientific.com/chf

ISSN: 3023-8951

Chaos and Fractals
Volume: 2 – Issue No: 2 (July 2025)

EDITORIAL BOARD

Editor-in-Chief
Dr. Dumitru Baleanu, Lebanese American University, LEBANON, dumitru.baleanu@lau.edu.lb

Associate Editors
Dr. Miguel A.F. Sanjuán, Universidad Rey Juan Carlos, SPAIN, miguel.sanjuan@urjc.es
Dr. René Lozı, University Cote d'Azur, FRANCE, rene.lozi@univ-cotedazur.fr
Dr. Martin Bohner, Missouri University of Science and Technology, USA, bohner@mst.edu

Editorial Board Members
Dr. Esteban Tlelo-Cuautle, Instituto Nacional de Astrofísica, MEXICO, etlelo@inaoep.mx
Dr. Abdurrahim Toktas, Ankara University, TURKIYE, toktasa@ankara.edu.tr
Dr. Denis Butusov, Saint Petersburg State Electrotechnical University, RUSSIA, butusovdn@mail.ru
Dr. Ahmet Zengin, Sakarya University, TURKIYE, azengin@sakarya.edu.tr
Dr. Jun Ma, Lanzhou university of Technology, CHINA, hyperchaos@163.com
Dr. Yunus Babacan, Erzincan Binali Yıldırım University, TURKIYE, ybabacan@erzincan.edu.tr
Dr. Haris Skokos, University of Cape Town, SOUTH AFRICA, haris.skokos_at_uct.ac.za
Dr. Jordan Hristov, University of Chemical Technology and Metallurgy, BULGARIA, hristovmeister@gmail.com
Dr. Marcelo Messias, São Paulo State University, BRAZIL, marcelo.messias1@unesp.br
Dr. Jacques Kengne, Université de Dschang, CAMEROON, kengnemozart@yahoo.fr
Dr. Ugur Erkan, Ankara University, TURKIYE, ugurerkan@ankara.edu.tr
Dr. Jawad Ahmad, Prince Mohammad Bin Fahd University, SAUDI ARABIA, jawad.saj@gmail.com
Dr. Lazaros Moysis, University of Nova Gorica, SLOVENIA, lazaros.moysis@ung.si
Dr. Bilel Selmi, Université de Monastir, TUNISIA, bilel.selmi@fsm.rnu.tn
Dr. Suo Gao, Dalian Polytechnic University, CHINA, gaosuo@dlpu.edu.cn
Dr. Abdullah Yesil, Bandirma Onyedi Eylül University, TURKIYE, ayesil@bandirma.edu.tr

Editorial Advisory Board Members
Dr. Fatih Ozkaynak, Fırat University, TURKIYE, ozkaynak@firat.edu.tr
Dr. Buğra Bağcı, Hitit University, TURKIYE, bugrabagci@hitit.edu.tr
Dr. Haris Calgan, Balıkesir University, TURKIYE, haris.calgan@balikesir.edu.tr

Language Editor
Dr. Mustafa Kutlu, Sakarya University of Applied Sciences, TURKIYE, mkutlu@subu.edu.tr

Technical Coordinator
Dr. Murat Erhan Cimen, Sakarya University of Applied Sciences, TURKIYE, muratcimen@subu.edu.tr

https://journals.adbascientific.com/chf/about/editorialTeam

ISSN: 3023-8951

Chaos and Fractals
Volume: 2 – Issue No: 2 (July 2025)

CONTENTS

https://journals.adbascientific.com/chf/issue/view/13

ADBA Chaos and Fractals
Cutting-Edge Scientific Solutions

e-ISSN: 3023-8951
RESEARCH ARTICLE
Vol.2 / **No.**2 / 2025 / **pp.**28-37
https://doi.org/10.69882/adba.chf.2025071

Attack-Resistant Chaotic Communication System in Non-ideal Physical Channel

Timur Karimov [α, β, 1], **Alexander Mikhailov** [α, 2], **Vyacheslav Rybin** [α, β, 3], **Varvara Sheptunova** [α, 4], **Ivan Babkin** [α, β, 5] and **Denis Butusov** [α, 6]
[α] Computer-Aided Design Department, Saint Petersburg Electrotechnical University "LETI", 197022 Saint Petersburg, Russia, [β]Youth Research Institute, Saint Petersburg Electrotechnical University "LETI", 197022 Saint Petersburg, Russia.

ABSTRACT

Coherent chaos-based communication is a developing technique for secure data transmission based on synchronization of chaotic oscillators at the transmitter and receiver sides, which is treated as a more secure method than non-coherent communication, chaotic symbolic dynamics, and other approaches. Nowadays, digital implementation of such systems allows high precision in parameter matching and sophisticated message recovery algorithms, though challenges remain: first, in adapting chaotic signals for non-ideal physical media, e.g., acoustic channels with frequency-dependent attenuation and noise, while, second, still providing the high level of security. The current study provides the implementation of a coherent chaotic communication system based on the Sprott Case S chaotic oscillator that meets these challenges. We utilize the modulation technique, minimizing changes in chaotic dynamics that may be captured by an intruder, propose an optimization of chaotic oscillator parameters to match channel characteristics and establish a signal normalization procedure to neutralize attenuation at the receiver side. Applying spectral and return map attacks, we show that the measures taken to counteract distortion in the path do not reduce the security of the transmission. In an experiment with a physical acoustic path, we demonstrate the practical operability of our approach.

KEYWORDS
Chaos-based communication
Acoustic communication system
Secure communications
Chaotic shift keying

INTRODUCTION

Chaos-based communication is an innovative approach for secure and efficient data transmission, utilizing the distinctive features of chaotic dynamics. This type of communication is based on chaotic oscillators, which are capable of producing deterministic signals of complex, aperiodic shape, resembling noise. Unlike conventional harmonic oscillators, chaotic oscillators have several nonlinear components in feedback, which leads to their sensitivity to initial conditions and unpredictability of the trajectory in time. Such signals are irregular, aperiodic, and have a wide spectrum. That is why these oscillators are considered promising carriers of information in communication systems, enabling reliable and secure information transfer across various physical media.

One of the key discoveries in chaotic systems was the phenomenon of synchronization (Pecora and Carroll 1990; Anishchenko *et al.* 1992), that is, the signals of two identical chaotic oscillators can be fully matched when a master-slave drive between oscillators is established. Pecora and Carroll proved that a necessary condition for synchronization is the negative values of all conditional Lyapunov exponents for the slave system, which means the stability of its trajectories with respect to the master system. The Pecora-Carroll synchronization method implies a proportional control, and due to its simplicity, it is used in lots of works, demonstrating that synchronization is possible even in the case of hyperchaos (Wang *et al.* 2010), multistability (Pisarchik *et al.* 2008), delayed signals (Eisencraft *et al.* 2012), mismatch of parameters, etc.

Manuscript received: 30 June 2025,
Revised: 22 July 2025,
Accepted: 22 July 2025.

[1]tikarimov@etu.ru
[2]aamikhailov@etu.ru
[3]vgrybin@etu.ru
[4]vesheptunova@etu.ru
[5]iababkin@etu.ru
[6]dnbutusov@etu.ru (**Corresponding author**)

Chaos synchronization has become the basis for coherent chaotic communication, which assume synchronization between transmitter and receiver, in contrast to non-coherent systems, which are based on the correlation or other types of analysis for message recovery (Kaddoum 2016). Coherent systems offer a higher level of secrecy, however, they are sensitive to noise, significantly affecting the detection accuracy. Filtering or error correction techniques may be required to maintain reliable performance. In coherent systems, the simplest modulation technique is chaotic masking (Oppenheim *et al.* 1992). An information signal $m(t)$ is added to the chaotic noise-like signal of the generator on the transmitter side, and the masking signal must be subtracted at the receiving side to recover $m(t)$. Alas, the security of such modulation is weak against existing attacks. In particular, adding the message $m(t)$ to the chaotic signal alters the power of the resulting signal, which may be estimated by power analysis of the transmitted signal. Practical modulation techniques include the chaotic shift keying (CSK), first presented by Parlitz *et al.* (1992). In CSK, information bits are transmitted by selecting one of the two chaotic generator modes according to the bit stream $m(t)$. On the receiver side, two copies of the oscillator attempt to synchronize with the received signal. The copy that synchronizes more accurately indicates the bit being transmitted.

Chaotic communication can be physically implemented using both analog and digital hardware. Initially, chaotic communication systems (CCS) were proposed in analog form, e.g. in Cuomo *et al.* (1993). Nowadays, digital electronics occupy researchers interest due to its high precision, compatibility with digital data, and the ability to support complex modulation and digital signal processing algorithms. Research on novel attractors for digital CCS, modulation schemes, microcontroller or FPGA implementations, and related topics remains an active field of study (Kolumbán *et al.* 1998), Wang (2018), Babajans *et al.* (2022), Bonny *et al.* (2024), Babajans *et al.* (2025). With that, just minor quantity of studies focus on issues of chaotic communication signals propagation and adaptation for media with non-ideal properties, besides presence of additive noise. Relevant researches consider chaotic hydroacoustic path (Bai *et al.* 2019), generalized medium with finite bandwidth, additive noise and delay in the communication channel (Eisencraft *et al.* 2012), medium with multi-path propagation, noise and chaotic interference (Baptista 2021), and some other media. In the latter study, Baptista reports the preservation of the largest Lyapunov exponent of a chaotic signal when it propagates in a medium, which is a strong argument for further development of CCS.

In our previous work (Rybin *et al.* 2023), we presented the practical implementation of CCS based on a 32-bit microcontroller. The signals in this system were transmitted through a wire, and considered disturbances included only additive white Gaussian noise. In the current study, we attempt to implement coherent CCS in an audible acoustic channel, which primarily assumes frequency-dependent dissipation and attenuation. The novelty and contribution of the study are as follows.

1. We identify the acoustic channel and then optimize the frequency and data transfer rate of the chaotic generators to better match physical channel properties.

2. The original mechanism to counteract signal attenuation is proposed, namely, normalization of the received signal to levels that corresponds to undisturbed signals generated by oscillators with the appropriate parameter sets.

3. By computer simulation and hardware-in-the-loop (HIL) implementation of the developed CCS, which uses physical acoustic path, we study bit error rate, transfer rate, and security of the designed communication system and draw conclusions about the necessity of signal pre-filtering and bit error correction mechanisms.

The paper is organized as follows: in Section 2, the description of the modulation scheme and hardware is provided, as well as the basic chaotic oscillator and secrecy estimate. Section 3 presents the results of the simulation and experimental investigation of the designed CCS prototype. Section 4 discusses obtained results and concludes the paper.

MATERIALS AND METHODS

Sprott Case S system and its parameterization

In 1994 J. Sprott found a number of simple chaotic systems in the form of third-order ordinary differential equations (Sprott 1994) that possessed different attractor topologies in the presence of only one kind (multiplication). The Case S is an attractor possessing one unstable saddle equilibrium position and remaining chaotic over a wide range of parameters, with its largest Lyapunov exponent in the large region of the parameter space where the chaotic dynamics is observed exceeding that of the other Sprott systems. This implies a rapid exponential divergence of trajectories, which is useful for generating a broadband noise-like signal. The Case S system equations can be written as

$$\begin{cases} \dot{x} = -x - ay \\ \dot{y} = x + z^2 \\ \dot{z} = b + x \end{cases} \tag{1}$$

With typical parameters ($a \approx 4, b \approx 1$), the maximum Lyapunov exponent for Case S is about 0.18, indicating a chaotic state. Unlike analog circuits, the system is easy to implement numerically, which was used in the study of digital direct chaotic communication. The Sprott S system is of special interest for communications because it remains chaotic even with coarse sampling. In addition, its chaotic oscillations have a complex spectral composition and a wide frequency range.

The investigation of dynamical behavior in the Sprott Case S system was conducted through a multi-parameter analysis combining bifurcation diagrams and Lyapunov spectrum to evaluate transitions between periodic and chaotic regimes under parameter variation. Simulation was performed using both 4-th order Ruge-Kutta and 2-nd order semi-implicit CD (Butusov *et al.* 2019; Rybin *et al.* 2025) methods to verify the absence of numerical artifacts. A two-dimensional bifurcation diagram (Fig. 1a) was calculated by varying parameters a and b, revealing intricate structures of periodic windows embedded within chaotic regions. Additionally, the corresponding Largest Lyapunov exponent estimation (Fig. 1b) provided quantitative insights into the system's sensitivity to initial conditions, with positive values of λ_1 delineating chaotic domains. To isolate the influence of parameter a, one-dimensional bifurcation diagram (Fig. 1c) and Lyapunov spectrum (Fig. 1d) were calculated by replacing parameter b by the linear relationship $b = f(a) = 0.0602a + 0.7308$, derived from the dashed trajectory in Figures 1a-b.

This parametric substitution enabled targeted exploration of dynamical transitions along specific parameter pathways, revealing abrupt period-doubling cascades and crises indicative of chaos emergence. Further, we will consider the single-parameter Sprott Case S oscillator:

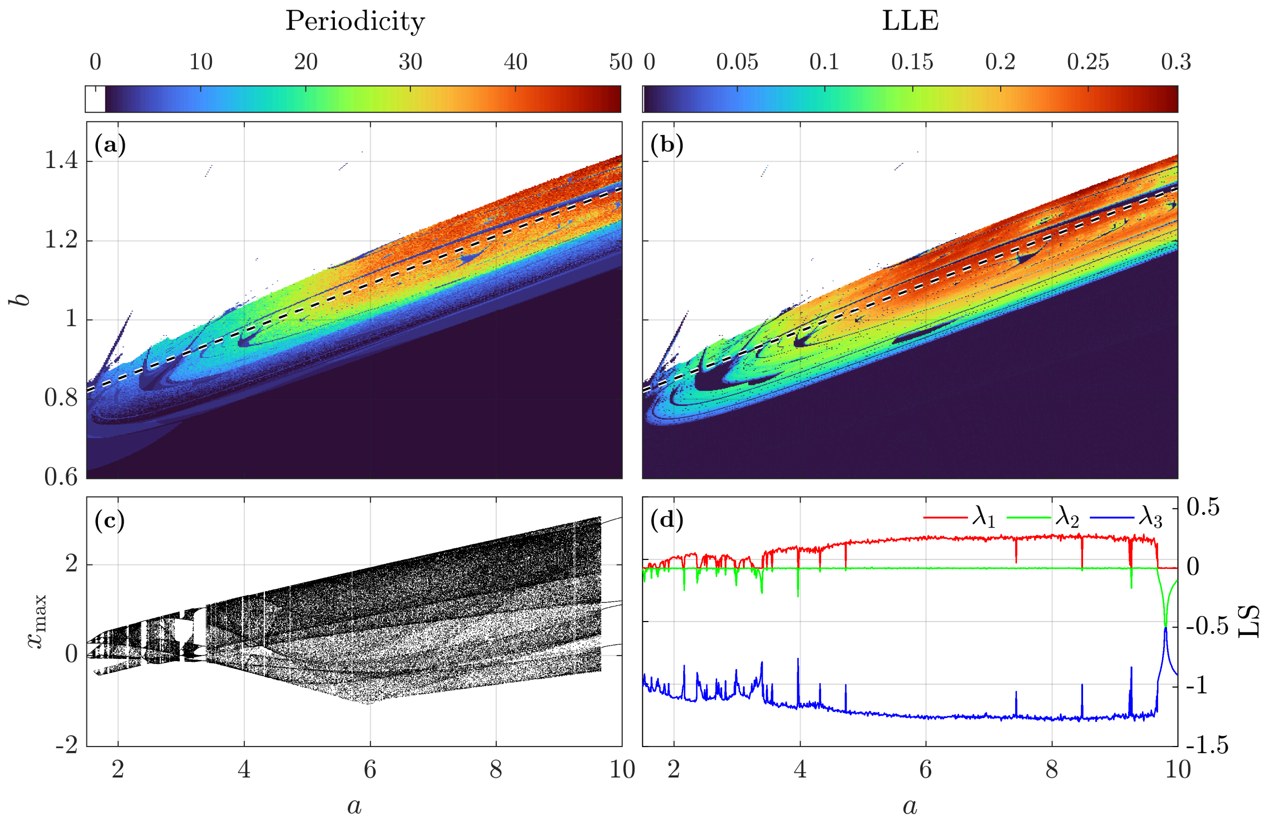

Figure 1 2D-Periodicity **(a)** and largest Lyapunov exponent **(b)** diagrams for Sprott Case S system, white color corresponds for unbound solution, black-white dash line corresponds for $b = f(a) = 0.0602a + 0.7308$. 1D-bifurcation **(c)** and Lyapunov spectrum **(d)** diagrams are calculated by varying parameter a with replacing parameter b by $f(a) = 0.0602a + 0.7308$.

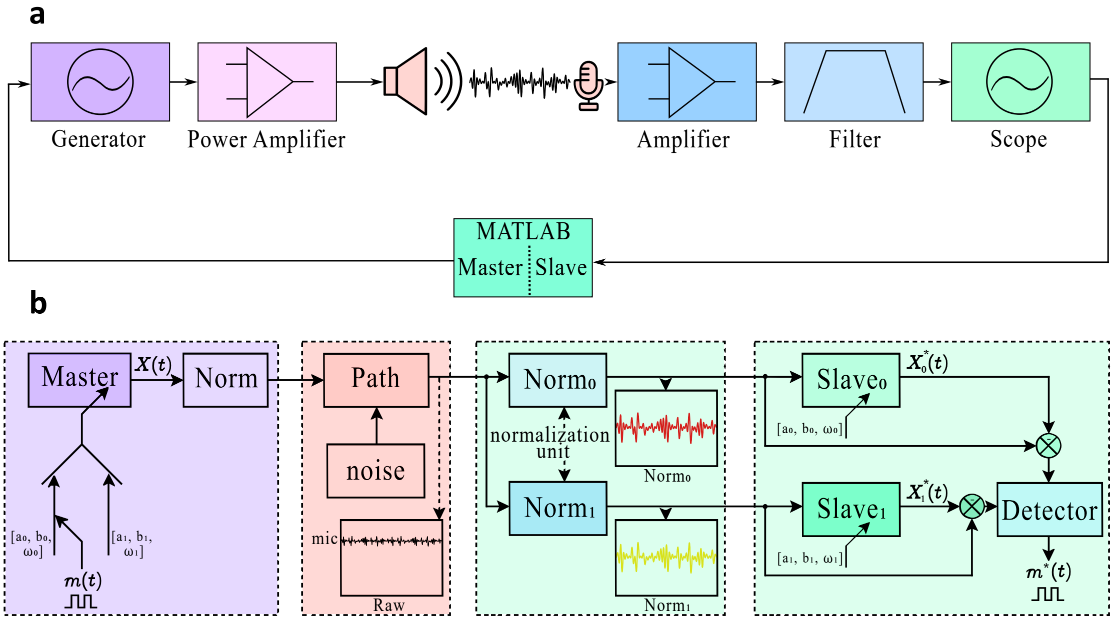

Figure 2 Schematic of the chaotic communication system with acoustic path. **a** Hardware-in-the-loop experiment with acoustic path implemented using physical devices, while receiver and transmitter are simulated in MATLAB; **b** detailed schematic of the communication system. The blocks of signal normalization set the waveform received from the path to those amplitudes and shifts, which correspond to the chaotic signals of system with given parameters

$$\begin{cases} \dot{x} = -x - ay \\ \dot{y} = x + z^2 \\ \dot{z} = 0.0602a + x + 0.7308 \end{cases} \tag{2}$$

Adaptation of chaotic system for non-ideal channel

Schematic of the proposed chaotic system and experiment is presented in Figure 2. For the acoustic channel research, a hardware-in-the-loop system was designed and implemented using a digital generator, speaker, microphone, and oscilloscope with signal recording functionality. As an audio frequency amplifier (AFA), a class D device based on chip TPA3118 is used, providing acoustic power up to 30 W per channel with a very low harmonic distortion. The observed distortion in the channel is caused by the small-sized speaker and, to a lesser extent, by low-cost piezoelectric microphone. The mic signal is pre-processed by an electric circuit based on MAX4466 amplifier.

The acoustic channel was measured by scanning with harmonic signals that cover the entire bandwidth, with synchronous recording of the emitted and received signals. In the subsequent automated processing of the experiment, noise multiplicative interference in the received signal was taken into account. The received signal was recorded from the output of the microphone amplifier as it was then fed into an analog or digital chaotic system as a synchronization signal. The Keysight Technologies 33210A signal generator was used to construct signals, and Rigol DS1104 four-channel digital oscilloscope was used for recording. As a result, frequency response of the channel $H(f_k)$ for the frequencies f_k was obtained.

Simulation of the channel was carried out using the signal $x(t_n)$ decomposition by fast Fourier transform, multiplication of the spectrum by the channel frequency response $\widetilde{H}(f_n)$ interpolated to a given frequency grid f_n, as only values for $H(f_k)$ are known, $f_n \neq f_k$, followed by the inverse Fourier transform to get signal in time domain. Notation t_n stands for discrete time $t_n = h \cdot n$, where $h = \Delta t$ is a time step, and n is the number of discrete sample.

$$\begin{aligned} X(f_n) &= \mathcal{F}\{x(t_n)\} = \sum_{n=0}^{N-1} x_n \cdot e^{-j\frac{2\pi}{N}kn}, \quad k = 0, \ldots, N-1 \\ Y(f_n) &= X(f_n) \cdot \widetilde{H}(f_n), \\ y(t_n) &= \mathcal{F}^{-1}\{Y(f_n)\} = \frac{1}{N}\sum_{k=0}^{N-1} Y_k \cdot e^{j\frac{2\pi}{N}kn}, \quad n = 0, \ldots, N-1 \end{aligned}$$

Mathematically, such transform is equivalent to the convolution of the signal $x(t)$ with impulse response of the path $h(t)$.

$$y(t_n) = x(t_n) * h(t_n)$$

The developed model was used to test propagation of Sprott Case S signal through the acoustic media.

To adopt the chaotic system oscillations frequency to the frequency range of the path, an acceleration coefficient ω is introduced:

$$\dot{\mathbf{x}} = \omega f(\mathbf{x})$$

With that, master-slave synchronization of systems (2) would be as follows:

$$\begin{aligned} &\begin{cases} \omega^{-1}\dot{x_m} = -x_m - ay_m \\ \omega^{-1}\dot{y_m} = x_m + z_m^2 \\ \omega^{-1}\dot{z_m} = 0.0602a + x_m + 0.7308 \end{cases} \\ &\begin{cases} \omega^{-1}\dot{x_s} = -x_s - ay_s \\ \omega^{-1}\dot{y_s} = x_s + z_s^2 \\ \omega^{-1}\dot{z_s} = 0.0602a + x_s + 0.7308 + k(\tilde{z}_m - z_s) \end{cases} \end{aligned} \tag{3}$$

Here, k is a synchronization coefficient, and $\tilde{z}_m$ is the master drive signal. If no channel is considered, $\tilde{z}_m = z_m$, otherwise $\tilde{z}_m = f_{path}(z_m)$, where f_{path} is a function which distorts the master signal. For the channel simulation, we use a combination of channel distortion with additive noise:

$$\tilde{z}_m(t_n) = z_m(t_n) * h(t_n) + \epsilon_{0,\sigma^2} \tag{4}$$

where ϵ_{0,σ^2} is an additive white Gaussian noise.

To estimate the effect of the channel model on the chaotic signal, the spectral difference Δ_f between two instancies of the chaotic signal before and after propagating through the channel may be estimated:

$$\Delta_f = RMS(\tilde{Z}_m(f_n) - Z_m(f_n)).$$

As another estimate, close to the practical operation of a coherent communication system, the RMS error of synchronization of two chaotic oscillators can be taken. Note that the distorted master signal is used to calculate the synchronization error, since the exact value of this signal is unknown at the receiver side.

$$\Delta_{t_n} = RMS(\tilde{z}_m(t_n) - z_s(t_n)).$$

Using the proposed approach, the optimization of Case S to frequency properties of the propagation path was performed, see Figure 3.

The results in Figure 3 show the consistency of both metrics Δ_{t_n} and Δ_f. The figure shows that there exists the range of parameters ω, for which the synchronization between master and slave systems has the lowest error. In this range, the distortion of the master signal spectrum is also minimal. Here and further, values of syncrhonization coefficients $k_0 = 4.6$ and $k_1 = 5.7$ were used for Slave 0 and Slave 1, respectively.

As the optimal value, $\omega^* = 2.6 \cdot 10^3$ was taken. This value is not the exact mathematical optimum but is accurate enough considering the inevitable discrepancy between model and real path and also may be varied, keeping synchronization at an acceptably fine level (we will use this option further). For a different chaotic system and a different physical path, the optimal ω value will differ, but the search procedure will be similar.

Modulation and demodulation

At the transmitter side: we use chaotic system parameters modulation to encode binary symbols '0' and '1'. Symbols are presented as parameter vectors $\mathbf{p}_0$ and $\mathbf{p}_1$, which may include all the parameters: a, b (as a function of a) and ω. The need for the last parameter to be modulated is presented in Figure 4. For '0' and '1', $a_0 = 4.65$ and $a_1 = 6.1$ were chosen. One may see that although the spectrum for both parameters is generally similar, the specific peak frequency values are significantly different, which may be easily captured by spectrogram analysis, see Figure 5(a).

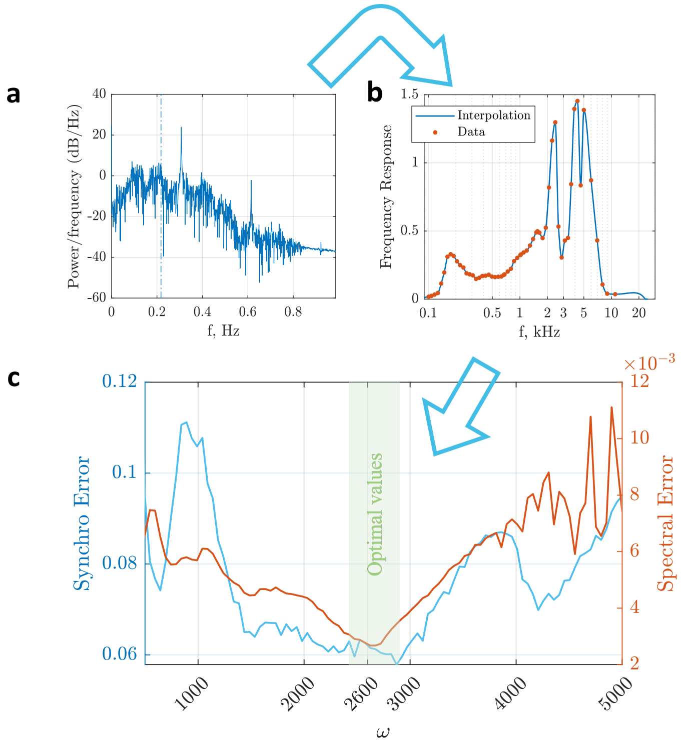

Figure 3 Optimization of parameter ω to find the best match between the channel frequency response and spectrum of Sprott Case S chaotic system: (a) Sprott Case S (2) spectrum, i.e. $\omega = 1$, (b) frequency response of the measured acoustic channel, (c) dependence of synchronization error between two identical chaotic oscillators when master signal was propagated through the channel Δ_{t_n}, and difference of spectra Δ_f between two instancies of chaotic signal before and after propagating through the channel, on ω.

Take the following parameter vectors: $\mathbf{p}_0 = [4.65, 1.11\omega^*]$ and $\mathbf{p}_0 = [6.1, 0.95\omega^*]$. In the first case, the median frequency of oscillations is increased, and in the second, decreased, to stay around optimal, feasible to the path frequency response. As a result, the data transmission becomes almost invisible for the spectral analysis, see Figure 5(b).

As presented in the schematic in Figure 2(b), each symbol waveform is normalized before being sent into a channel. The reason may be seen in Figure 1(c): the amplitude of the signal also changes with variation of a. Normalized waveforms are glued together using the cross-fade function to get smooth transitions between symbol waveforms.

At the receiver side: the signal is first re-normalized to return it back to the appropriate amplitude and shift equal to those of an undistorted signal. Before communication is established, these parameters are found numerically for each of the parameter vectors $\mathbf{p}_i$:

$$A_i = \max_{t \in [0,T]} |z(t)_i| \tag{5}$$

$$C_i = \frac{1}{T} \int_0^T z(t)_i \, dt \tag{6}$$

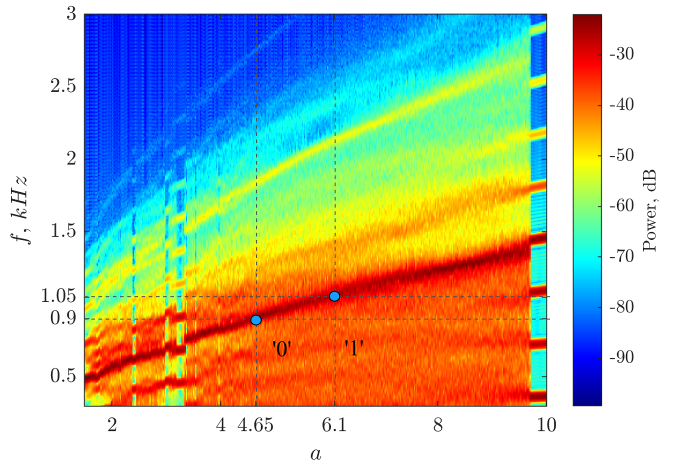

Figure 4 Bifurcation spectral diagram of Sprott Case S chaotic system adopted for physical channel with $\omega = 2.6 \cdot 10^3$.

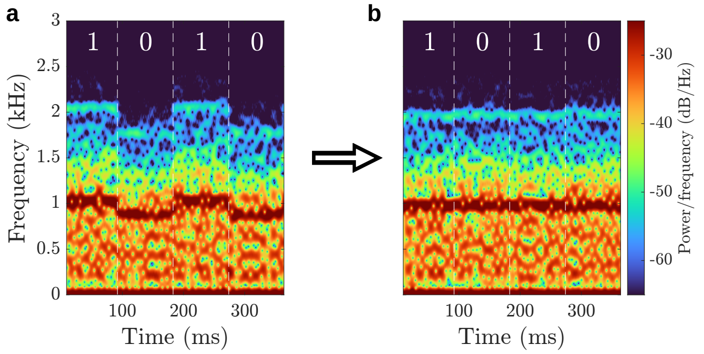

Figure 5 Spectrogram of the message '1010' transmitted before and after including ω in vector of modulated parameters.Spectrogram in **b** shows that spectral attack cannot be applied to decrypt the message.

After reading input signal from the channel, the signal is normalized to $[-1, 1]$:

$$z_{\text{norm}}(t) = 2 \cdot \left(\frac{z(t) - z_{\min}}{z_{\max} - z_{\min}} \right) - 1 \tag{7}$$

where $x_{\min} = \min x(t)$, $x_{\max} = \max x(t)$.

Then, the signal is amplified and shifted:

$$\tilde{z}(t)_i = A_i \cdot z_{norm}(t) + C_i \tag{8}$$

where A is the scale coefficient, C is the vertical shift.

The detector determines which of the two oscillators at the receiver side, with the parameter vectors $\mathbf{p}_0$ and $\mathbf{p}_1$, is more accurately synchronized with the input signal and decides which symbol is being transmitted. If the synchronization error exceeds a certain threshold, the detector recognizes this as the absence of a transmission in the channel.

Scheme of the experiment: is presented in Figure 2, relating the communication system to the broader class of chaotic shift keying systems. As is shown in block diagram, a Generator initiates the process by producing a signal generated previously in MATLAB software by master oscillator. The signal is then amplified through a Power Amplifier, transmitted using a Speaker, captured by a Microphone and further conditioned by a dedicated Amplifier.

This amplified signal passes through a Filter, likely designed to remove unwanted frequencies or noise, ensuring the signal meets the desired spectral characteristics. The filtered output is processed digitally by MATLAB software, where slave mathematical systems are simulated fed by this signal, and a message is decoded. The Master oscillator (labeled as $x(t)$) generates the primary signal, which undergoes parameters switching between sets (a_0, b_0, ω_0) and (a_1, b_1, ω_1). Then that signal is normalized and passed through a Path to Slave subsystems. The schematic references two Slave oscillators: Slave 0 and Slave 1, while demodulation is performed by analyzing synchronization errors on each of the slave oscillators.

Secrecy estimation

Quantified return map analysis (QRMA): is the further development of return map analysis (RMA), which has been widely used to attack chaotic communication systems. It was first demonstrated by Pérez and Cerdeira (1995) to extract messages masked by chaos. The method is that certain characteristic points (e.g., extrema) are extracted from the received chaotic signal and the dependence between their values is mapped. The resulting return transform reflects the dynamic properties of the chaos generator; a difference in the generator parameters (e.g., when transmitting 0 or 1) leads to a change in the type of return transform, which makes it possible to identify the transmitted bit. Nevertheless, the classical method of return transforms is qualitative: by visually distinguishing segments in the plane, it is clear that the parameters are changing. Until recently, there have been no reliable ways to quantify these differences, making it difficult to assess the level of secrecy and compare different chaos modulation methods in terms of security. However, without a quantitative measure, it is difficult to objectively judge the effectiveness of methods that are proposed to increase the complexity of return transform analysis. In this study, the distinguishability between chaotic signals is assessed by QRMA (Rybin *et al.* 2022) which is implemented as follows. For a given chaotic signal $x(t)$, local extrema (peaks X_m and valleys Y_m) are identified to compute recurrence points. These points form coordinates for the return map, which is discretized into an $N \times N$ grid to create a histogram matrix $H \in \mathbb{R}^{N\times N}$. To compare two signals (e.g., transmitted binary symbols), their histograms X and Y are analyzed using the formula:

$$\Delta_{i,j} = \|X_{i,j} - Y_{i,j}\| \cdot \|\Theta(X_{i,j}) - \Theta(Y_{i,j})\|, \quad i,j \in [1,N],$$

where Θ is the Heaviside step function and $\epsilon \in \mathbb{N}$ acts as a noise threshold:

$$\theta(x) = \begin{cases} x & \text{if } x \geq \epsilon \\ 0 & \text{if } x < \epsilon \end{cases}.$$

The normalized difference metric D is calculated as:

$$D = \sum_{i=1}^{N} \sum_{j=1}^{N} \frac{\theta(\Delta_{i,j})}{\theta(X_{i,j}) + \theta(Y_{i,j})}.$$

This metric quantifies the percentage difference between signals, with higher values indicating distinguishable modulation.

Amplitude return maps, which rely on peak-valley amplitudes, are unsuitable for systems with amplitude distortions (e.g., hydroacoustic channels). Instead, phase return maps focus on interpeak/intervalley intervals, preserving frequency characteristics unaffected by amplitude noise. For phase return maps, intervals between consecutive peaks X_m and valleys Y_m are defined as:

$$W_{2,m} = T(X_m) - T(X_{m-1}), \quad U_{2,m} = T(Y_m) - T(Y_{m-1}),$$

where $T(\cdot)$ denotes the timestamp of an extremum. Symmetric coordinates are computed as:

$$A_{t,m} = \frac{W_{2,m} + U_{2,m}}{2}, \quad B_{t,m} = W_{2,m} - U_{2,m},$$

$$C_{t,m} = \frac{W_{2,m+1} + U_{2,m+1}}{2}, \quad D_{t,m} = U_{2,m} - W_{2,m+1}.$$

Plotting A vs. $-B$ and C vs. $-D$ generates the phase return map. This approach captures temporal dynamics, making it robust to amplitude distortions.

RESULTS

Simulation

Simulation of the proposed CCS was performed in MATLAB environment using Runge-Kutta 4-th order method and simulation time $h \approx 2 \cdot 10^{-5}$ (the particular value was chosen with respect to ω). For this task, a class called *ChaoticCommunication* was developed for keeping all the parameters of the simulated system, which included functions for simulation of all necessary steps, i.e.: preliminary system parameters estimation (e.g. scaling factors for further normalization), message waveform generation, path simulation, signal normalization at the receiver side, synchronization of slave oscillators with the normalized signal, message detection based on the synchronization error, messaging quality estimation, and spectral and return map analyses.

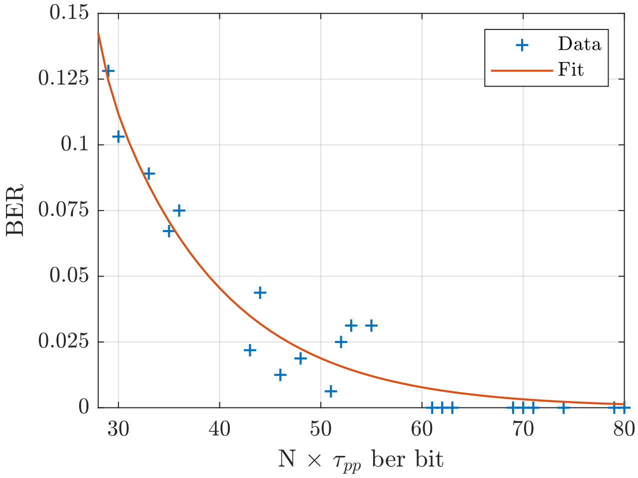

Figure 6 Estimation of bit error rate for different bit duration times. N denotes the duration in pseudo-periods (τ_{pp}).

To establish a stable difference between the transmitted bits in conditions of signal distortion, the transmission time of one bit was investigated. Figure 6 shows the dependence of the bit error rate (BER) on the length of the transmitted message. Simulation and analysis were performed for a number of 32-bit messages. Along the horizontal axis, the length of the transmitted bit is shown in pseudo-periods $\tau_{pp} = f_{mean}^{-1}$. One can see a local minimum around the transmitted bit length of 50 pseudo-periods, which means that some 32-bit messages can be transmitted without errors at the transfer rate of 11 bit/sec, see Figure 7 for an example. For Sprott Case S and $\omega = 2.6 \cdot 10^3$ approximately $t_{bit\,duration} \approx$ 90 ms, which results in a sample rate of 11 bit/sec, which is a feasible rate for implementations based on microcontrollers (Rybin *et al.* 2023). However, from Figure 6 it follows that a bit duration

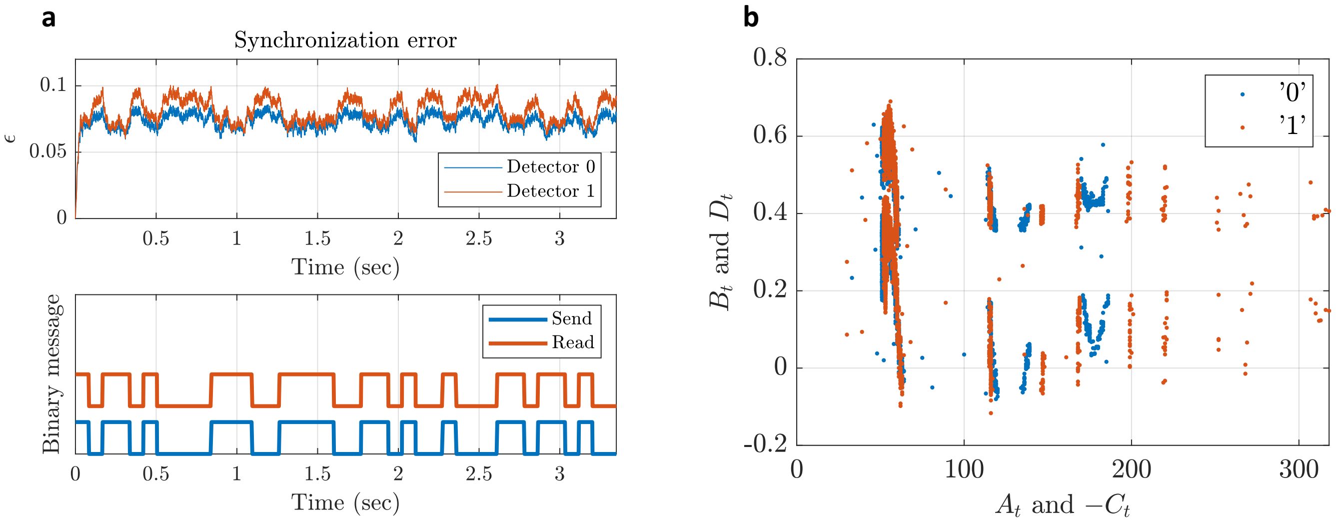

Figure 7 Simulation data on the chaotic communication system with acoustic path. **a** Synchronization error and binary messages (sent and received) for the communications simulated in MATLAB with bit duration $50 \times \tau_{pp} \approx 90$ ms. The relative synchronization error between '0' and '1' for $t_{bit\,duration} = 50\tau_{pp}$ is about 16%. **b** Estimation of amplitude-phase QRMA in simulated path: $\Delta_{0,1} = 12\%$

of at least 80 pseudo-periods must be taken to establish reliable communication. With the established parameters of the designed acoustic communication system, this results in message rates below 7 bits/sec.

Experiment

The experiment was set up as follows. The waveform with the embedded message was generated in MATLAB and then written to a CSV file. This file was then read by an arbitrary waveform generator and played back in real time. The signal from the generator was fed to a power amplifier driving the speaker. The acoustic signal from the speaker was picked up by a chip-based microphone module with a preamplifier and then recorded on an oscilloscope in CSV file. This file was then read by MATLAB, and the recorded signal was substituted for the computer-generated one when simulating the communication system.

The photograph of the experiment, as well as the results of the message transmission and comparison of the frequency response between simulated and real path are presented in Figure 8. Particular models of the hardware items used are listed in the caption.

According to the experimental results, e.g., comparison of the synchronization error and the QRMA plot, we may conclude that the real path presents noticeably greater difficulties in establishing reliable communication than in the simulation. In particular, the synchronization error in the real path is almost two times higher. At the rate of 11 bit/sec, long messages were not successfully transmitted without error, but we observed messages of 8 bits length transmitted without errors.

Comparison in the terms of secrecy

Table 1 summarizes the key properties of the CCS with developed modulation technique and without introduced enhancements. The experiments were carried out using simulation of the proposed chaotic communication system based on Sprott Case S oscillator. Comparison with other works known from the literature may be irrelevant due to the variety of algorithms used to evaluate secrecy (if they are ever applied). Recent works applying some estimates of the chaotic communication systems secrecy include: Mushenko *et al.* (2020); Bonny *et al.* (2023); Babkin *et al.* (2024); Bonny and Al Nassan (2024); Rybin *et al.* (2025), etc. One may note that estimates are often proposed in graphical rather than numerical form, e.g. in the form of return maps, histograms, and autocorrelation plots. Also, none of the mentioned works consider physical communication channel.

DISCUSSION

The key finding of this study is that even in conditions of strong nonlinear distortion of the transmitted signal in a direct chaotic communication system, it is possible to select transmitter parameters that would form an attack-resistant communication system utilizing simple Pecora-Carroll synchronization technique. Meanwhile, the current study just partly highlights the issues that need to be solved towards creating a practically applicable direct chaotic communication system.

Limitations: of the study are related to the fact that the demonstration of the system's operation is performed for one chaotic system and one set of parameters. The dependence of communication quality on distance between transmitter and receiver, as well as the influence of different types of physical channels and interferences on communication quality were not addressed. We believe that our results open a wide field for further research. Although in our example the communication system was possible to operate with a signal directly received from a path, signal restoration is desirable. In its simplest form, it may consist of denoising, which may be performed by various methods, including promising approaches, i.e., ensemble intrinsic time-scale decomposition (Voznesensky *et al.* 2022), synchronization with sequential cascade of slave oscillators (Butusov *et al.* 2018), etc. More sophisticated restoration methods may include the receiver signal convolution with reciprocal impulse response of the path, model-based identification and by using other approaches.

Practical implementation: of the proposed chaotic communication system should consider that one information symbol is transferred during several decades of pseudo-periods $\tau_{pp} = f_{mean}^{-1}$. Taking into account the Nyquist frequency, which should be at least 10 points

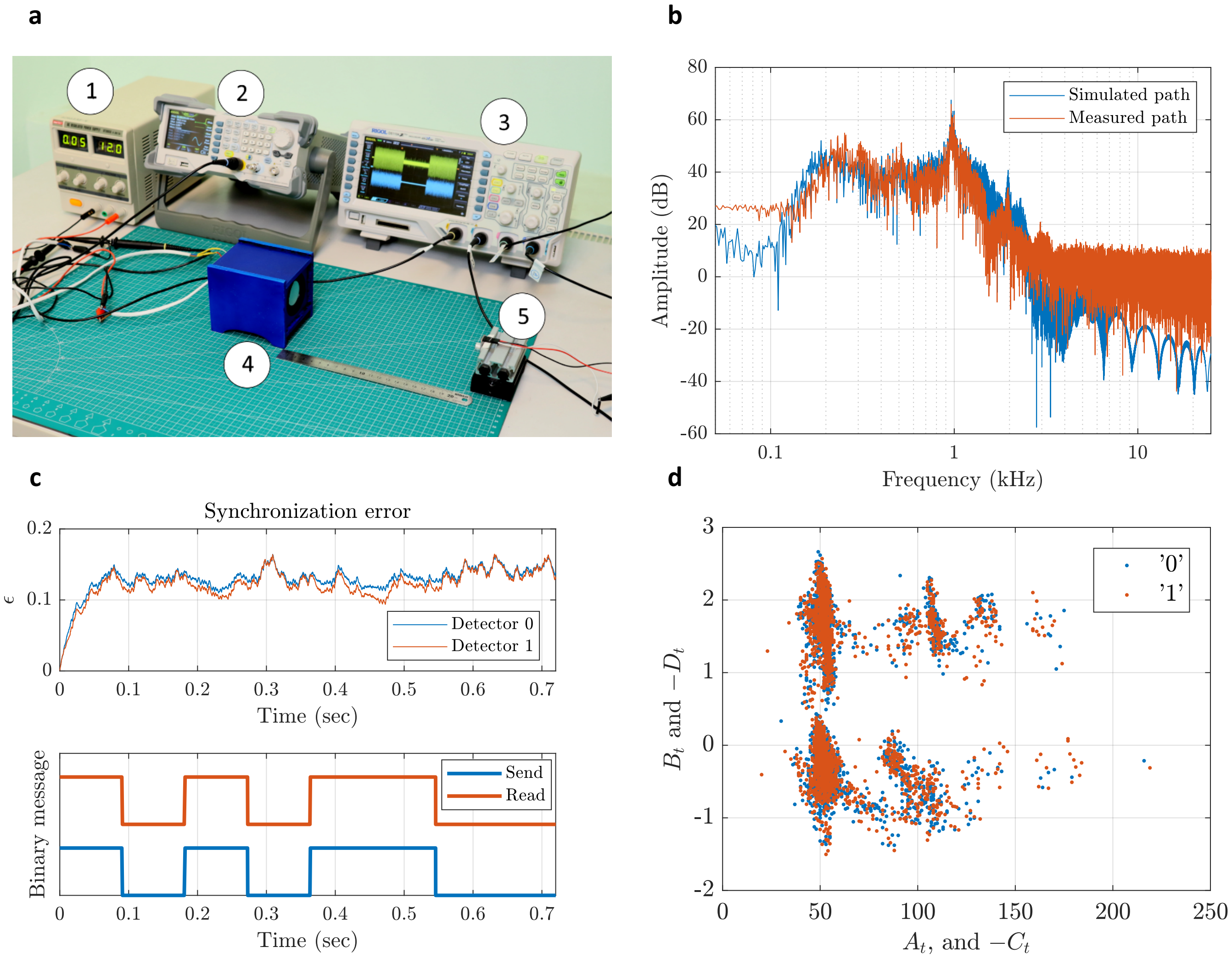

Figure 8 Experimental data on the chaotic communication system with acoustic path. **a** Photograph of the experiment. Here: (1) power supply for the amplifier of the speaker; (2) Rigol DG1032Z arbitrary signal generator reproducing the chaotic waveform with embedded message; (3) Rigol DS1054 oscilloscope used to capture both input of audio amplifier (yellow) and microphone output (blue) signals; (4) audio frequency amplifier based on chip TPA3118 and speaker in a single casing; (5) piezoelectric microphone with MAX4466 amplifier. **b** Spectra of the chaotic waveforms in simulated and measured paths. **c** Synchronization error and message waveforms for bit duration $50 \times \tau_{pp} \approx 90$ ms in physical acoustic path. The relative synchronization error between ’0’ and ’1’ for $t_{bit\,duration} = 50\tau_{pp}$ is about 7.5%. **d** Estimation of amplitude-phase QRMA in physical path: $\Delta_{0,1} = 5.2\%$.

Table 1 Secrecy estimates of chaotic communication system with proposed and standard modulation techniques

Vector of modulated parameters	References	Phase QRMA	Relative entropy difference between bits ’0’ and ’1’	Pearson correlation between information message and energy in peak band (p-value)
$[a, b = f(a), \omega]$	This work	11.2%	1.09%	0.041
$[a, b = f(a)]$, $\omega = 2.6 \cdot 10^3$	This work	67.5%	15%	0.53
$[a]$, $b = 1.01$, $\omega = 2.6 \cdot 10^3$	Cuomo *et al.* (1993); Kaddoum (2016)	76.8%	17.3%	0.51

in the pseudo-period, the sampling rate of the system should be hundreds of times higher than the bitrate. Accounting for the need to use signal processing algorithms, FPGAs are the optimal digital platform for implementing direct chaotic communication systems.

Convergence issues are also to be considered when choosing the particular chaotic oscillator and sample rate. With that, utilization of fast time-reversible synchronization (Butusov *et al.* 2025) could significantly improve the transfer rate of coherent CCS, which also needs further study.

Applicability: of the proposed CCS in its current stage of development includes communication channels with moderate signal distortion and low to moderate transfer rates in which the information message must be disguised as noise. In underwater environments, this technology offers advantages in mitigating interference and minimizing ecological disruption with population-level consequences, particularly for animals with a limited geographic range (Trickey *et al.* 2022). E.g., it may be applied in navigation buoys and for short messages between the mothership and underwater self-acting robots.

CONCLUSION

In the current study, a new direct-chaotic communication system based on the Sprott Case S oscillator was proposed, which is characterized by high entropy values and a broadband noise-like signal providing high transmission security. One of the key features of the proposed system is the normalization block which aims to overcome signal attenuation in the physical channel. By optimizing oscillator dynamics, including tuning frequency scaling factor $\omega = 2.6 \times 10^3$, and modulation parameters $a_0 = 4.65$, $a_1 = 6.1$, we achieved synchronization stability and minimized spectral distortion, ensuring reliable data recovery and maintaining robust security. Experimental results show the applicability of the proposed approach for implementation in real-world physical applications with a relatively low data transfer rate of 7-11 bits/sec, which was demonstrated in a prototype. The Quantified Return Map Analysis (QRMA) revealed only 5-12% distinguishability between transmitted symbols, demonstrating a high level of secrecy.

This study bridges theoretical synchronization principles with practical implementation, validating coherent chaotic communication systems as a feasible alternative to conventional means in constrained environments. Future efforts to integrate advanced signal restoration and develop FPGA prototypes are still necessary steps towards practical application, but the current results solidify the foundation for chaos-based communication in real-world scenarios.

Acknowledgments

This study is supported by Russian Science Foundation, grant number 24-71-10064.

Ethical standard

The authors have no relevant financial or non-financial interests to disclose.

Availability of data and material

Not applicable.

Conflicts of interest

The authors declare that there is no conflict of interest regarding the publication of this paper.

LITERATURE CITED

Anishchenko, V., T. Vadivasova, D. Postnov, and M. Safonova, 1992 Synchronization of chaos. International Journal of Bifurcation and Chaos **2**: 633–644.

Babajans, R., D. Cirjulina, and D. Kolosovs, 2025 Field-programmable gate array-based chaos oscillator implementation for analog–discrete and discrete–analog chaotic synchronization applications. Entropy **27**: 334.

Babajans, R., D. Cirjulina, D. Kolosovs, and A. Litvinenko, 2022 Quadrature chaos phase shift keying communication system based on vilnius chaos oscillator. In *2022 Workshop on Microwave Theory and Techniques in Wireless Communications (MTTW)*, pp. 5–8, IEEE.

Babkin, I., V. Rybin, V. Andreev, T. Karimov, and D. Butusov, 2024 Coherent chaotic communication using generalized runge–kutta method. Mathematics **12**: 994.

Bai, C., H.-P. Ren, M. S. Baptista, and C. Grebogi, 2019 Digital underwater communication with chaos. Communications in Nonlinear Science and Numerical Simulation **73**: 14–24.

Baptista, M. S., 2021 Chaos for communication. Nonlinear Dynamics **105**: 1821–1841.

Bonny, T. and W. Al Nassan, 2024 Optimizing security and cost efficiency in n-level cascaded chaotic-based secure communication system. Applied System Innovation **7**: 107.

Bonny, T., W. Al Nassan, and A. Sambas, 2024 Comparative analysis and fpga realization of different control synchronization approaches for chaos-based secured communication systems. PLOS ONE **19**: 1–33.

Bonny, T., W. A. Nassan, S. Vaidyanathan, and A. Sambas, 2023 Highly-secured chaos-based communication system using cascaded masking technique and adaptive synchronization. Multimedia Tools and Applications **82**: 34229–34258.

Butusov, D., T. Karimov, A. Voznesenskiy, D. Kaplun, V. Andreev, *et al.*, 2018 Filtering techniques for chaotic signal processing. Electronics **7**: 450.

Butusov, D., V. Rybin, and A. Karimov, 2025 Fast time-reversible synchronization of chaotic systems. Physical Review E **111**: 014213.

Butusov, D. N., V. Y. Ostrovskii, A. I. Karimov, and V. S. Andreev, 2019 Semi-explicit composition methods in memcapacitor circuit simulation. International Journal of Embedded and Real-Time Communication Systems (IJERTCS) **10**: 37–52.

Cuomo, K. M., A. V. Oppenheim, and S. H. Strogatz, 1993 Synchronization of lorenz-based chaotic circuits with applications to communications. IEEE Transactions on circuits and systems II: Analog and digital signal processing **40**: 626–633.

Eisencraft, M., R. Fanganiello, J. Grzybowski, D. Soriano, R. Attux, *et al.*, 2012 Chaos-based communication systems in non-ideal channels. Communications in Nonlinear Science and Numerical Simulation **17**: 4707–4718.

Kaddoum, G., 2016 Wireless chaos-based communication systems: A comprehensive survey. IEEE access **4**: 2621–2648.

Kolumbán, G., G. Kis, Z. JaKo, and M. P. Kennedy, 1998 Fm-dcsk: A robust modulation scheme for chaotic communications. IEICE Transactions on Fundamentals of Electronics, Communications and Computer Sciences **81**: 1798–1802.

Mushenko, A., J. Dzuba, A. Nekrasov, and C. Fidge, 2020 A data secured communication system design procedure with a chaotic carrier and synergetic observer. Electronics **9**: 497.

Oppenheim, A., K. Cuomo, S. Isabelle, and G. Wornell, 1992 Signal processing in the context of chaotic signals . In *Acoustics, Speech, and Signal Processing, IEEE International Conference on*, volume 4, pp. 117–120, Los Alamitos, CA, USA, IEEE Computer Society.

Parlitz, U., L. CHUA, L. KOCAREV, K. HALLE, and A. SHANG, 1992 Transmission of digital signals by chaotic synchronization. International Journal of Bifurcation and Chaos **02**: 973–977.

Pecora, L. M. and T. L. Carroll, 1990 Synchronization in chaotic systems. Phys. Rev. Lett. **64**: 821–824.

Pérez, G. and H. A. Cerdeira, 1995 Extracting messages masked by chaos. Phys. Rev. Lett. **74**: 1970–1973.

Pisarchik, A., R. Jaimes-Reategui, and J. Garcia-Lopez, 2008 Synchronization of multistable systems. International Journal of Bifurcation and Chaos **18**: 1801–1819.

Rybin, V., I. Babkin, Y. Bobrova, M. Galchenko, A. Mikhailov, *et al.*, 2025 Variable-step semi-implicit solver with adjustable symmetry and its application for chaos-based communication. Mathematics **13**.

Rybin, V., D. Butusov, E. Rodionova, T. Karimov, V. Ostrovskii, *et al.*, 2022 Discovering chaos-based communications by recurrence quantification and quantified return map analyses. International Journal of Bifurcation and Chaos **32**: 2250136.

Rybin, V., T. Karimov, O. Bayazitov, D. Kvitko, I. Babkin, *et al.*, 2023 Prototyping the symmetry-based chaotic communication system using microcontroller unit. Applied Sciences **13**.

Sprott, J. C., 1994 Some simple chaotic flows. Phys. Rev. E **50**: R647–R650.

Trickey, J. S., G. Cárdenas-Hinojosa, L. Rojas-Bracho, G. S. Schorr, B. K. Rone, *et al.*, 2022 Ultrasonic antifouling devices negatively impact cuvier's beaked whales near guadalupe island, méxico. Communications Biology **5**: 1005.

Voznesensky, A., D. Butusov, V. Rybin, D. Kaplun, T. Karimov, *et al.*, 2022 Denoising chaotic signals using ensemble intrinsic time-scale decomposition. IEEE Access **10**: 115767–115775.

Wang, H., Z. zhi Han, and Z. Mo, 2010 Synchronization of hyperchaotic systems via linear control. Communications in Nonlinear Science and Numerical Simulation **15**: 1910–1920.

Wang, S., 2018 Dynamical analysis of memristive unified chaotic system and its application in secure communication. IEEE Access **6**: 66055–66061.

How to cite this article: Karimov, T., Mikhailov, A., Rybin, V., Sheptunova, V., and Butusov, D. Attack-Resistant Chaotic Communication System in Non-ideal Physical Channel. *Chaos and Fractals*, 2(2), 28-37, 2025.

Chaos and Fractals
Cutting-Edge Scientific Solutions

e-ISSN: 3023-8951
RESEARCH ARTICLE
Vol.2 / **No.**2 / 2025 / **pp.**38-42
https://doi.org/10.69882/adba.chf.2025072

Dynamical Analysis of Barium Titanate Crystal in Alternative Voltage RL Circuit

Guy Joseph Eyebe[*,1], **Justin Mibaile**[α,2], **Rolande Tsapla Fotsa**[β,3], **Gambo Betchewe**[§,4] **and Alidou Mohamadou**[§,5]
[*]Department of Oil and Gas Mechanical Engineering, National Advanced School of Mines and Petroleum Industries, P.O. Box 08, Kaele, Cameroon, [α]Department of Renewable Energy, National Advanced School of Engineering, University of Maroua, P.O. Box 46, Maroua, Cameroon, [β]Department of Mechanical Engineering, College of Technology, University of Buea, P.O. BOX 63, Buea, Cameroon, [§]Department of Physics, Faculty of Science, The University of Maroua, P.O. Box 814, Maroua, Cameroon.

ABSTRACT This brief paper theoretically investigates the dynamical characteristics of ferroelectric materials, specifically barium titanate $(BaTiO_3)$ crystal in alternative voltage resistor (R) and inductor (L) circuit. The theory of Landau-Ginzburg-Devonshire and Kirchhoff's law are used to derive the equation for the polarization field in the $BaTiO_3$ crystal. The Averaging method is applied to obtain an approximate analytical solution, and the numerical simulations of the system's equations is used to confirm the analytical obtained solution. The Melnikov method is used to investigate horseshoe chaos and the critical amplitude of excitation. The phase portraits, Poincaré sections, local maxima and greatest Lyapunov exponent are drawn to confirm the results obtained with Melnikov method.

KEYWORDS
Barium titanate crystal
Polarization
Averaging method
Melnikov method
Horseshoe chaos

INTRODUCTION

Ferroelectric materials are materials that exhibit spontaneous and reversible electrical polarization under the influence of an electric field. $BaTiO_3$ is an example of a ferroelectric material that has been extensively studied for its unique properties (Chen *et al.* 2018, 2024). The $BaTiO_3$ can be produced using various methods including room temperature synthesis, hydrothermal processes, bioinspired and biosynthetic approaches, sonochemical techniques, molten salt reactions, and peptide or phage-templated strategies, each enabling control over particle size, morphology, and phase with potential for green, scalable, and low-cost production (Chen *et al.* 2018, 2024). Chen *et al.* (2018) demonstrated that $BaTiO_3$ nanoparticles could be synthesized at room temperature conditions under ambient pressure. The hydrothermal synthesis of $BaTiO_3$ utilizing $NaTi_3O_6(OH)-(H_2O)_2$ nanowires, conducted by controlling temperature, alkalinity, and time was studied by (Chen *et al.* 2024).

Studies on the dielectric and ferroelectric properties of$BaTiO_3$ single crystals using the Landau phenomenological thermodynamic potential have been extensively conducted. Wang et al. suggested that when using the sixth-power free energy expansion of the thermodynamic potential, remarkably different values of the fourth-power coefficient are required to adequately reproduce the nonlinear dielectric behavior of the paraelectric phase and the electric field-induced ferroelectric phase, respectively (Wang *et al.* 2007). To develop the Landau-Devonshire potential of the perovskites $BaTiO_3$, the Gibbs free energy of $BaTiO_3$ single crystal has been expanded up to 10^{th}-order polynomial by (Ma *et al.* 2017). Large studies have shown that barium titanate crystals can be integrated into silicon and photonic platforms to enable high-performance, low-voltage, and high-speed electro-optic modulators and tunable dielectric devices for advanced integrated circuits and photonic applications. Picavet et al. presented a low-cost, high-throughput, and flexible method for integrating highly textured $BaTiO_3$ films on photonic integrated circuits, enabling large-scale fabrication of nanophotonic $BaTiO_3$ thin-film modulators (Picavet *et al.* 2024).

Xiong *et al.* (2014) showed how Ferroelectric $BaTiO_3$ thin films on silicon-on-insulator platforms has promising potential for broadband applications, with modulation bandwidth in the gigahertz regime. (Nayak *et al.* 2014) showed that $BaTiO_3$ multipods with high permittivity and low dielectric loss could be easily prepared and used for charge storage devices and electronic applications. Nonlinear dissipative dynamics, which underlie most real systems, have gained significant attention from theoretical and experimental researchers over the past few decades. Examples

---

Manuscript received: 21 May 2025,
Revised: 17 July 2025,
Accepted: 17 July 2025.

[1] yusufeyebe@gmail.com (**Corresponding author**)
[2] thejust7@yahoo.fr
[3] tsapla.fotsa@ubuea.cm
[4] gambobetch@yahoo.fr
[5] alidoumohamadou@gmail.com

of physical designs that are modeled by these dynamics include Josephson junctions, lasers etc.. A common characteristic of all these devices is that they can display surprisingly irregular behaviors when a control parameter is slightly modified. (Oikawa *et al.* 2024) analyzed chaotic behavior in Josephson junction for high-quality random-number generation. (Shuai *et al.* 2025) conducted research on chaos dynamic characteristics of multiple interactive Josephson junction application. (Kang *et al.* 2024) revealed a new scenario for the transition of solitons to chaos in a mode-locked fiber laser: The modulated subharmonic route.

The main reason justifying such interest lies in the fact that $BaTiO_3$ crystal is a good candidate for designing integrated circuits. The aim of this paper involves the determination of horseshoe chaos in the barium titanate crystal in alternative voltage RL circuit. Following this introduction, the paper is organized as follows: in section 2, we derive the governing equation of the circuit, the averaging method is applied to obtain an approximate analytical solution, and the numerical simulation of the system's equations is used to confirm the analytical results. The Melnikov method is used to investigate the Hamilton chaos, The phase portraits, Poincare sections, local maxima, and greatest Lyapunov exponent are drawn. Finally, section 3 is devoted to summarising the most important conclusions.

ANALYSIS OF $BaTiO_3$ CRYSTAL IN ALTERNATIVE VOLTAGE RL CIRCUIT

The $BaTiO_3$ crystal connected to alternative voltage RL circuit is considered in this paper (Figure 1). A simple case at temperatures in the vicinity of only the cubic-tetragonal phase transition where nonlinear behavior becomes stronger due to the strong nonlinearity of the restoring force and other effects and phase transitions (orthorhombic, rhombohedral) are negligible (Wang *et al.* 2007; Ma *et al.* 2017). We thus restrict the analysis in this paper to the case where the electromechanical coupling coefficient is very weak so that the dynamics of the electrical component is sufficient to capture all the properties of the system. The Landau model, completed by Devonshire (Coelho 1979; Waser and Lohse 1998; Starkov *et al.* 2022) thermodynamically describes the phase transitions by postulating that the free energy associated with the displacement of the dipoles in a crystal is a Taylor series development as a function of the the spontaneous polarization P. If we consider that it is subjected to an electric field, an additional energy term is added. Using Gibbs free energy of the $(BaTiO_3)$ crystal and Applying Kirchhoff's law, the equation for the polarization field in the crystal can be derived as

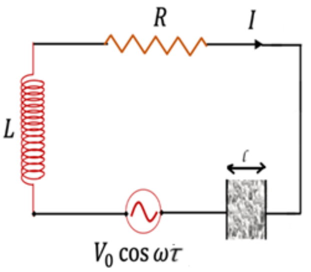

Figure 1 $BaTiO_3$ crystal connected to alternative voltage RL circuit.

$$U_R + U_L + U_{Crystal} = V_0 \cos\omega\tau, \tag{1}$$

with $U_R = RI(\tau) = R\frac{dq(\tau)}{d\tau}$, $U_L = L\frac{dI(\tau)}{d\tau} = L\frac{d^2q(\tau)}{d\tau^2}$, $U_{Crystal} = \left[\alpha(T)\bar{P} - \beta\bar{P}^3 + \gamma\bar{P}^5\right] l$, where $I(\tau)$ and $q(\tau)$ are electric current and charges. $\bar{P}$ is spontaneous polarization, R, L, l, A are respectively RL constants, width and surface of crystal. V_0 is amplitude of sinusoidal excitation with frequency w, α, β and γ are constant coefficients except α which depends on the temperature. The coefficient $(-\beta)$ instead of β is used in the equation to take into account its negative sign found in the literature (Wang *et al.* 2007; Ma *et al.* 2017). Equation (1) can be rewritten in the following form

$$\frac{d^2\bar{P}}{d\tau^2} + \frac{R}{L}\frac{d\bar{P}}{d\tau} + \frac{l}{LA}\left[\alpha(T)\bar{P} - \beta\bar{P}^3 + \gamma\bar{P}^5\right] = \frac{V_0}{A}\cos w\tau, \tag{2}$$

To put the equation (2) into a dimensionless form, let us use the rescaling :

$$\begin{aligned} \omega_0 = \tfrac{\beta^2 l}{4\gamma LA}, t = \omega_0\tau, P = \bar{P}\sqrt{\tfrac{2\gamma}{\beta}}, \mu = \tfrac{R}{L\omega_0}, \\ \alpha_T = \tfrac{l}{AL\omega_0^2}\alpha(T), \Omega = \tfrac{\omega}{\omega_0}, V = \tfrac{V_0}{AL\omega_0^2}\sqrt{\tfrac{2\gamma}{\beta}}. \end{aligned} \tag{3}$$

By substituting Eq. (3) in Eq. (2), it becomes :

$$\frac{d^2P}{dt^2} + \mu\frac{dP}{dt} + \alpha_T P - 2P^3 + P^5 = V\cos(\Omega t) \tag{4}$$

The potential energy associated with the system of Eq. (4) is

$$U(P) = \frac{1}{2}\alpha_T P^2 - \frac{1}{2}P^4 + \frac{1}{6}P^6 + C, \tag{5}$$

where C is a constant depending of characteristic potential. The shape of the potential given by Eq. (5) is shown in Figure 2 for different values of α_T.

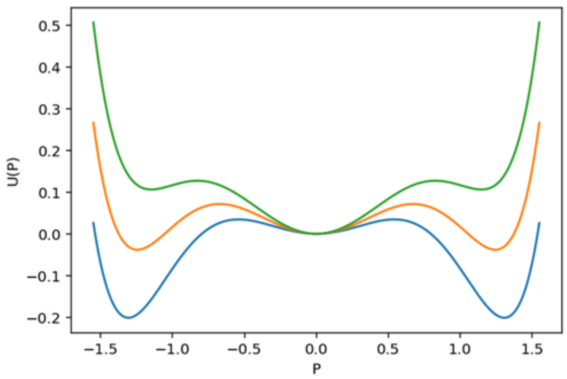

Figure 2 Shape of the potential for given value of α_T: (α_T =0.5 (blue), α_T =0.7 (red), α_T =0.9 (green)).

Figure 2 has three wells and two humps. By decreasing the value of α_T, the depth of three increase.

Averaging method

The averaging Method is used in this paper since the $BaTiO3$ crystal in Fig.1 is subjected to a weakly periodic forcing like an AC electric field, resulting in both rapid oscillations and slower changes due to the medium's nonlinear response. It effectively reduces the original system, which may be analytically intractable due to its nonlinearity and time dependence, into an averaged system that describes the slow evolution of amplitude and phase (Sanders *et al.* 2007). The averaging method is used in Eq. (4)

to obtain approximate solutions and confirm these mathematical results through numerical simulations of the system's equations. Figure 3 illustrates the curve of the amplitude of P versus frequency for both the analytical and numerical solutions. The solution can be written as

$$\begin{aligned} &P\left(t\right)=a\left(t\right)\cos\left(\theta\left(t\right)\right), \theta\left(t\right)=\sqrt{\alpha_T}t+\phi\left(t\right) \\ &\tfrac{dP}{dt}=-a\left(t\right)\sqrt{\alpha_T}\sin\left(\theta\left(t\right)\right), \end{aligned} \tag{6}$$

where a and θ represent the amplitude and the phase which are slow-varying functions of t. Substituting Eq. (6) into Eq. (4) and average over the period $T=2\pi/\sqrt{\alpha_T}$, we obtain

$$\begin{aligned} &\tfrac{da}{dt}=-\tfrac{\mu}{2}a \\ &\tfrac{d\phi}{dt}=-\tfrac{3a^2}{4\sqrt{\alpha_T}}+\tfrac{5a^4}{16\sqrt{\alpha_T}}, \end{aligned} \tag{7}$$

By integrating each component of Eq. (7), it is obtained

$$\begin{aligned} &a\left(t\right)=a_0\exp\left(\tfrac{-\mu t}{2}\right) \\ &\phi\left(t\right)=\phi_0-\tfrac{3a_0^2}{4\mu\sqrt{\alpha_T}}\left(1-\exp\left(\tfrac{-\mu t}{2}\right)\right) \\ &+\tfrac{5a_0^4}{32\mu\sqrt{\alpha_T}}\left(1-\exp\left(\tfrac{-2\mu t}{2}\right)\right). \end{aligned} \tag{8}$$

Now to confirm this mathematical result we apply numerical integration of Eq. (4) using robust four order Runge-Kutta and depict both numerical and analytical solutions.

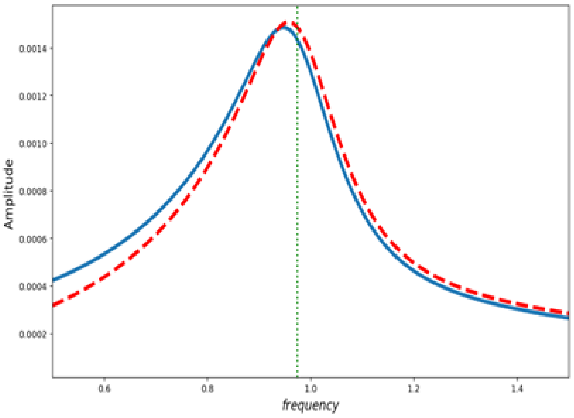

Figure 3 Amplitude versus frequency (analytical : Blue and numerical : Red).

Figure 3 shows in blue line, the variation of the amplitude of the solution (6) where a_0, ϕ_0 are constants. The curve in red is the same amplitude obtained from the numerical simulation of Eq. (4). One finds a good agreement between the mathematical and numerical results.

Melnikov method

To establish the conditions for the emergence of chaos in Eq. (4), the Melnikov method is applied (Melnikov 1963; Wiggins 1990). Consider the dynamical equation of a given system written in vector form

$$\dot{u}=g_0\left(u\right)+\varepsilon g_p\left(u,t\right), u=\left(P,\frac{dP}{dt}\right), \tag{9}$$

$$\begin{aligned} &g_0\left(u\right)=\left(\begin{array}{c}\frac{dP}{dt}\\ -\sqrt{\alpha_T}P+2P^3-P^5\end{array}\right), \\ &g_p\left(u,t\right)=\left(\begin{array}{c}0\\ -\mu\frac{dP}{dt}+V\cos\left(\Omega t\right)\end{array}\right), \end{aligned} \tag{10}$$

where u is the state vector, g_0 is the vector field chosen with the non-perturbed Hamiltonian and g_p is a periodic perturbation function. Let's consider a Hamiltonian system that has saddle points connected by a separatrix or heteroclinic orbit, or possibly just a single hyperbolic saddle point with a homoclinic orbit. When a perturbation g_p is introduced, the orbits of the system become altered. If the perturbed and unperturbed manifolds intersect transversally, the geometry of the basin of attraction may turn fractal. This fractal structure indicates a high sensitivity to initial conditions, which is a proof of chaotic behavior. The Melnikov's theorem which gives the condition for the fractal basin boundary can be given as follows [9,10].

$$\begin{aligned} &M\left(t_0\right)=\int_{-\infty}^{+\infty}g_0\left(u\left(t\right)\right)\wedge g_p\left(u\left(t\right),t+t_0\right), \\ &M\left(t_0\right)=0, \tfrac{dM(t_0)}{dt}\neq 0. \end{aligned} \tag{11}$$

The Hamiltonian of Eq. (3) is defined by

$$H_0(P,\frac{dP}{dt})=\frac{1}{2}\left(\frac{dP}{dt}\right)^2+\frac{\alpha_T}{2}P^2-\frac{1}{2}P^4+\frac{1}{6}P^6. \tag{12}$$

Given the shape of the potential U, one can make the assumption that the system possesses homoclinic orbits connecting saddle points and heteroclinic orbits connecting hyperbolic saddle points. The mathematical derivation of this Melnikov function can be found in (Tchoukuegno *et al.* 2002; Lenci *et al.* 1999) and Applying this Melnikov condition gives the following conditions for the appearance of chaos:

$$\begin{aligned} &V_{cr}^{het}\geq\left[\tfrac{(2\chi+1)}{(1-\chi^2)^{1/2}}\left(\sin^{-1}(\chi)+\tfrac{\pi}{2}\right)+2+\chi\right]. \\ &\tfrac{\mu P_u Y}{8\Omega\pi(\chi+1)}\sinh\tfrac{2\Omega}{Y}, \\ &V_{cr}^{Ho}\geq\left[\tfrac{(2\chi+1)}{(1-\chi^2)^{1/2}}\left(\sin^{-1}(\chi)-\tfrac{\pi}{2}\right)+(2+\chi)\right]. \\ &\tfrac{\mu P_u Y}{32\Omega\pi(\chi+1)}\tfrac{1}{\sinh\left(\frac{2\Omega}{Y}\right)}, \\ &Y=P_u^2\left(2\left(\rho^2-1\right)\right)^{1/2}, \chi=\tfrac{5-3\rho^2}{3\rho^2-1}, \rho=P_s/P_u. \end{aligned} \tag{13}$$

where V_{cr}^{Ho} and V_{cr}^{het} are critical values of voltage respectively for homoclinic and heteroclinic orbits, Ps and Pu stand for stable and unstable equilibrium points. These conditions establish the threshold amplitudes of the supply voltage above which horseshoe chaos occurs. Figures 4 and 5 illustrate the conditions for homoclinic and heteroclinic orbits in the (Ω, V) plane for different values of α_T. The area above the line represents values of Ω and V that lead to unpredictable or chaotic behavior, while the area below the line corresponds to regular behavior.

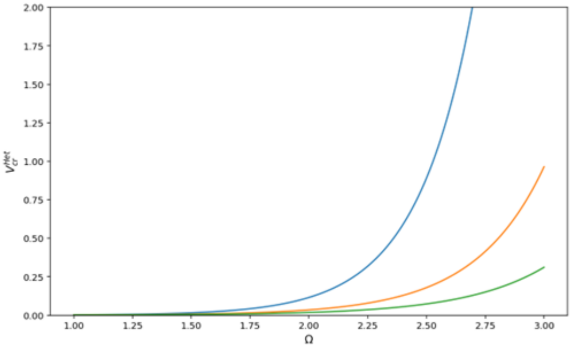

Figure 4 Critical value of voltage V_{cr}^{het} for given value of α_T : (α_T =0.3 (green), α_T =0.15 (red) and α_T =0.1 (blue)).

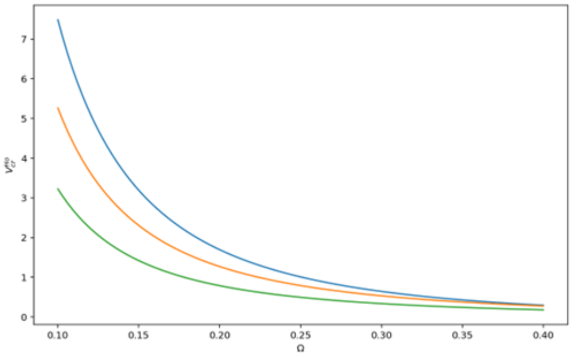

Figure 5 Critical value of voltage V_{cr}^{ho} for given value of α_T : (α_T =0.3 (green), α_T =0.15 (red) and α_T =0.1 (blue)).

In Figures 4 and 5, a variation of the critical value of voltage as a function of Ω are depicted. This is illustrated for different values of the parameter α_T. It is clear that the the critical value of ac- voltage in relation to Ω, which signifies the threshold for the onset of chaos, is significantly affected by the parameter α_T. As shown in Figure 4, a decrease in the parameter α_T results in a reduction of the chaotic domain for heteroclinic orbits. Figure 5 illustrates that a lower value of α_T enhances stability and narrows the chaotic region. To test the validity of these results, Fig. 6 is depicted, to confirm the analytical predictions of chaotic illustrated in Figs. 4 and 5. The phase portraits, Poincaré sections are depicted in Fig. 6, with parameters set to $\alpha_T = 0.04$, $\mu = 1.1$, $V = \Omega = 3.5$, $V = \Omega = 2.5$ with initial condition $(P(0) = 0.5, dP(0)/dt = 0.0)$. Figure 6 supports the validity of the analytical study presented in section 2.2 and visually represented in Figs. 4 and 5, demonstrating the presence of zones exhibiting chaotic and regular dynamics.

Figure 7 presents the local maxima of P and its corresponding greatest Lyapunov exponent (GLE) versus the parameter V.

Figure 7 (a) presents bistable limit cycle, period doubling route to chaotic region with windows of periodic characteristics, coexistence between limit cycle and chaotic characteristics and limit cycle, respectively. GLE of Figure 7 (b) confirms the dynamical characteristics found in Fig. 7 (a). The dynamical characteristics found in Fig. 7 are depicted in Fig. 8.

Bistable limit cycle is shown in Fig. 8 (a). Figures 8 (b) and (c) present two different shapes of chaotic characteristics. The coexistence between limit cycle and chaotic characteristics is illustrated in Fig. 8 (d).

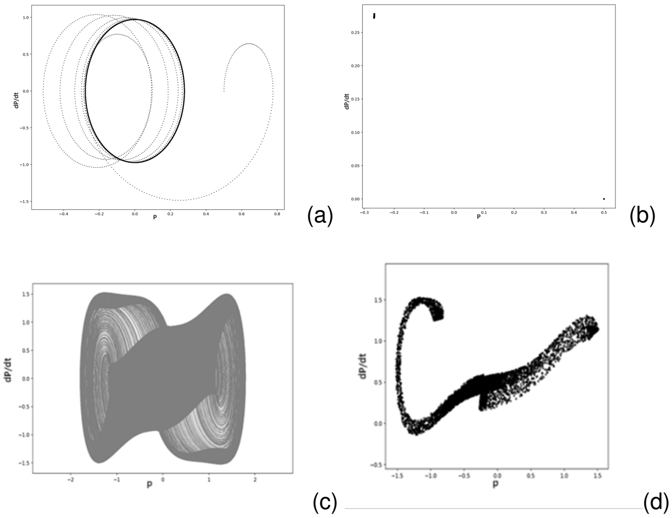

Figure 6 Phase portraits and Poincare sections $(\alpha_T = 0.04, \mu = 1.1)$: (a-b) $V = \Omega = 3.5$, (c-d) $V = \Omega = 2.5$. The curves are obtained by using the initial conditions $(P(0), dP(0)/dt) = (0.5, 0.0)$.

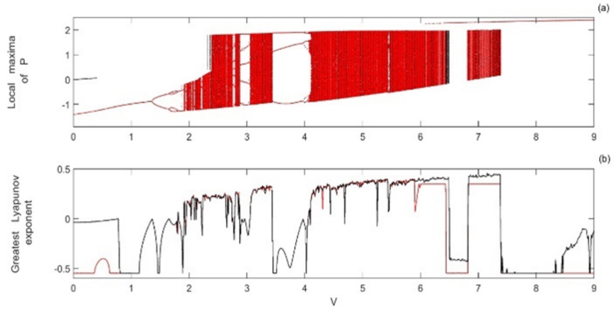

Figure 7 Local Maxima of P and its corresponding GLE versus the parameter V for $\alpha_T = 0.04$, $\mu = 1.1$ and $\Omega = 2.5$. Black dots (curves) are obtained by increasing the parameter V while red dots (curves) are obtained by decreasing the parameter V.

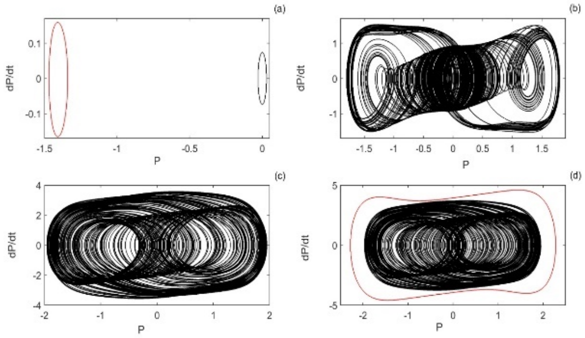

Figure 8 Phase portraits for given values of V $(\alpha_T = 0.04, \mu = 1.1)$: (a) $V = \Omega = 0.2$, (b) $V = \Omega = 2.5$, (c) $V = \Omega = 6$ and (d) $V = \Omega = 6.48$. The black curves are obtained by using the initial conditions $(P(0) = 0.01, dP(0)/dt = 0.01)$ while the red curves are obtained by using the initial conditions $(P(0) = 5.0, dP(0)/dt = 0.01)$.

CONCLUSION

This paper investigated dynamical characteristics in barium titanate crystal in alternative voltage RL circuit using the averaging method, Melnikov method and numerical simulations. The averaging method was applied to obtain an approximate analytical solution and the numerical simulations of the system's equations was used to confirm the analytical results. Good agreement between the analytical and numerical results was found. The Melnikov was demonstrated that the critical values of alternative voltage which delimits the boundary between chaotic and non-chaotic regimes is dependent to the structural parameter of the crystal. Numerical verifications using phase plots, Poincaré maps, local maxima and the greatest Lyapunov exponent supported the analytical prediction of chaotic behavior. This study yielded practical design information for chaos-resistant integrated circuits. Generalization of this study to also include the thermal-dependent part of circuit is needed for the further development of chaos control in complex circuits.

Ethical standard

The authors have no relevant financial or non-financial interests to disclose.

Availability of data and material

Not applicable.

Conflicts of interest

The authors declare that there is no conflict of interest regarding the publication of this paper.

LITERATURE CITED

Chen, S., B. Han, X. Chen, F. Xu, and G. Wang, 2024 Hydrothermal synthesis and morphology control mechanism of batio$_3$ from nati$_3$o$_6$(oh)(h$_2$o)$_2$ precursors. Ceramics International **50**: 21779–21787.

Chen, T., J. Meng, S. Wu, J. Pei, Q. Lin, *et al.*, 2018 Room temperature synthesized batio$_3$ for photocatalytic hydrogen evolution. Journal of Alloys and Compounds **754**: 184–189.

Coelho, R., 1979 *Physics of dielectrics for Engineers*. Elsevier Scientific Publishing Company, Amsterdam.

Kang, H., A. Zhou, Y. Zhang, X. Wu, B. Yuan, *et al.*, 2024 Observation of optical chaotic solitons and modulated subharmonic route to chaos in mode-locked laser. Physical Review Letters **133**: 263801.

Lenci, S., G. Menditto, and A. Tarantino, 1999 Homoclinic and heteroclinic bifurcations in the non-linear dynamics of a beam resting on an elastic substrate. International Journal of Non-Linear Mechanics **34**: 615–632.

Ma, Z., L. Xi, H. Liu, F. Zheng, H. Gao, *et al.*, 2017 Ferroelectric phase transition of batio$_3$ single crystal based on a tenth order landau-devonshire potential. Computational Materials Science **135**: 109–118.

Melnikov, V., 1963 On the stability of the center for some periodic pertubations. Trans. Moscow Math. Soc. **12**: 1–57.

Nayak, S., B. Sahoo, T. Chaki, and D. Khastgir, 2014 Facile preparation of uniform barium titanate (batio$_3$) multipods with high permittivity: impedance and temperature dependent dielectric behavior. RSC Advances **4**: 1212–1224.

Oikawa, D., H. Komatsu, K. Tsuzuki, H. Andoh, and T. Tsukamoto, 2024 Chaotic behavior in josephson junction for high-quality random-number generation. Journal of Applied Physics **136**: 123909.

Picavet, E., E. Lievens, K. De Geest, H. Rijckaert, E. Fernandez, *et al.*, 2024 Integration of solution-processed batio$_3$ thin films with high pockels coefficient on photonic platforms. Advanced Functional Materials **34**: 2403024.

Sanders, J. A., F. Verhulst, and J. Murdock, 2007 *Averaging methods in nonlinear dynamical systems*. Springer Science and Business, New York.

Shuai, W., W. Litian, X. Yulong, L. Dan, and L. Xueming, 2025 Research on chaos dynamic characteristics of multiple interactive josephson junction application. AIP Advances **15**: 035336.

Starkov, I. A., M. A. Mishnev, and A. S. Starkov, 2022 The equation of state for metal-doped ferroelectrics within the weiss model. Journal of Advanced Dielectrics **12**: 2250011.

Tchoukuegno, R., B. N. Nbendjo, and P. Woafo, 2002 Resonant oscillations and fractal basin boundaries of a particle in a ϕ^6 potential. Physica A: Statistical Mechanics and its Applications **304**: 362–378.

Wang, Y., A. Tagantsev, D. Damjanovic, N. Setter, V. Yarmarkin, *et al.*, 2007 Landau thermodynamic potential for batio$_3$. Journal of Applied Physics **101**: 104115.

Waser, R. and O. Lohse, 1998 Electrical characterization of ferroelectric, paraelectric, and superparaelectric thin films. Integrated Ferroelectrics **21**: 27–40.

Wiggins, S., 1990 *Introduction to the applied Nonlinear dynamic systems and chaos*. Springer, New York.

Xiong, C., W. Pernice, J. Ngai, J. Reiner, D. Kumah, *et al.*, 2014 Active silicon integrated nanophotonics: ferroelectric batio$_3$ devices. Nano letters **14**: 1419–1425.

How to cite this article: Eyebe, G. J., Mibaile, J., Fotsa, R. T., Betchewe, G., and Mohamadou, A. Dynamical Analysis of Barium Titanate Crystal in Alternative Voltage RL Circuit. *Chaos and Fractals*, 2(2), 38-42, 2025.

Chaos and Fractals
Cutting-Edge Scientific Solutions

e-ISSN: 3023-8951
RESEARCH ARTICLE
Vol.2 / **No.**2 / 2025 / **pp.**43-49
https://doi.org/10.69882/adba.chf.2025073

Synergistic Construction of High-Performance S-Boxes Based on Chaotic Systems: A Paradigm Shift in Cryptographic Security Design

Zaid Abdulsattar Abdulrazaq [*,1], **Harith Ghanim Ayoub** [α,2] **and Hakam Zaidan** [*,3]
[*]Technical Engineering College for Computer and AI / Mosul, Northern Technical University (NTU), Nineveh, Iraq, [α]Technical Management Institute, Northern Technical University (NTU), Nineveh, Iraq.

ABSTRACT Exchange of information between two nodes is a big issue in intenet these days. Multiple cryptosystems employed for this porpose with various mathmatical approaches. Most of these approaches uitilize subsitutions and pemutations. The subsituation S-box is a look up table that exchange x bits input with y bits output is incharge of substitution approach. The build of S-box with stong cryptographic power is important in recent cryptosystems. In this paper a novel approach for building robust and dynamic S-box with compound multi-dimentional chaotic systems. Lorenze and henon maps employed for construction of strong S-Box with multiple security performance metrics :non-linearity(NL), Strict Avalanche Criterion (SAC), Bit-Independence Criterion (BIC), Linear-Probability (LP) and differential-Probability (LP).The results showed that proposed S_box is will be powerfull for modern cryptosystems.

KEYWORDS
Cryptography
S-box
Security
Chaotic map
Nonlinearity

INTRODUCTION

Recently, secure data communication and encryption have attracted great concern due to the rapid growth in wireless communication technology and its applications (Asghar *et al.* 2022; Al-Turjman and Zahmatkesh 2022; Sirohi *et al.* 2023; Rahman *et al.* 2023; Khoshafa *et al.* 2024). In fact, the substitutive permutation operation is one of the basic criteria in the Advanced Encryption Standard and other symmetric-key cryptosystems, namely block and stream ciphers, to resist different attacks (Ali *et al.* 2022a; Farooq *et al.* 2022; Knežević 2023). Earlier, many S-box constructions have been done using various techniques such as algebraic, cryptographic, mapping, heuristic, non-linear, chaos, and machine learning among others. It is known that designing high-performance S-boxes is a complex, challenging, and NP-hard problem (Xun *et al.* 2024; Ekwueme *et al.* 2024; Picek and Jakobovic 2022; Bavdekar *et al.* 2022). Notably, a good S-box should satisfy various cryptographic properties to enhance security without any computational overhead. Such security properties are non-linearity, differential uniformity, bit independence criterion, branch number, strict avalanche criterion, and linear approximation probability among others (Waheed *et al.* 2023; Alqahtani *et al.* 2023; Ali *et al.* 2024; Mahboob *et al.* 2023).

It is worth mentioning here that the notion of chaos is completely different from that of noise. Chaos has irregular, unpredictable deterministic dynamics, which exhibit rich and intricate patterns, while the time evolution of a chaotic system depends on its initial conditions with a positive Lyapunov exponent (Progonatı 2023; Zelinka and Senkerik 2023; Frank 2024). Due to such properties, chaos has become an evolving concept in many scientific and engineering applications. These applications include cryptography, secure communication, image processing, electrochemistry, biology, quantum mechanics, pattern formation, and control among others. Notably, chaos-based encryption reveals that a chaotic system can create a key space to improve the security between end users (Abba *et al.* 2024; Hwang *et al.* 2023; Ilyas *et al.* 2022; Rahman *et al.* 2022).

The key contributions of this work are as follows:

1. Introduction of Multi-Dimensional Chaotic Maps for S-Box Design: The proposed method introduces an S-Box constructed using multi-dimensional chaotic maps, specifically utilizing the Lorenz and Henon chaotic systems.

Manuscript received: 11 January 2025,
Revised: 22 April 2025,
Accepted: 2 May 2025.

[1] zaid.a.abdulrazzaq@ntu.edu.iq (**Corresponding author**)
[2] harithga@ntu.edu.iq
[3] hakam_m_zaidan@ntu.edu.iq

2. Enhanced Resistance Against Linear Attacks: The proposed S-Box demonstrates a high level of non-linearity, significantly improving its resistance to linear cryptanalysis attacks.

3. Comprehensive Randomness Testing:

    - NIST Test Suite: The S-Box passes the NIST randomness tests with P-values significantly greater than 0.01, indicating robust security properties.
    - Distribution Tests: Results show P-values deviating substantially from a uniform distribution, highlighting the unpredictability of the S-Box values.
    - Dieharder Tests: The generated S-Box achieves high pass percentages, further validating its randomness and suitability for cryptographic use.

4. Suitability for Modern Cryptography: The results of this research make the proposed S-Box highly suitable for modern cryptosystems, as evidenced by the strong performance in the aforementioned security tests.

5. Comparative Performance Analysis: A comparative study with existing S-Box designs demonstrates that the proposed S-Box outperforms others in terms of key performance metrics, establishing it as a superior choice for cryptographic applications.

With the advent of the big data era, wired and wireless communication technology has explosively developed. This requires more and more secure encryption and decryption algorithms and the design of S-boxes. Due to the weaknesses of S-boxes, they need to be more secure and robust (Naseer *et al.* 2024; Al-Dweik *et al.* 2022; Indumathi and Sumathi 2022; Razaq *et al.* 2023; Ye and Chen 2024). Chaotic systems as design rules for S-boxes are particularly important in the field of information security. Therefore, the excellent performance of S-boxes is of paramount significance to the building. It is also of vital significance to both the building of chaotic systems and the design of a secure and robust block cipher system (Manzoor *et al.* 2022; Farah *et al.* 2020; Alsaif *et al.* 2023; Gohar 2023; Hoseini *et al.* 2022). The Henon map and the Lorenz chaotic system are two famous chaotic systems. The study of these two systems is also very important. The construction of excellent S-boxes has always been a particularly difficult problem. A constructive framework consisting of ten corresponding operations is used to construct a novel paradigm shift method of S-boxes (Long and Wang 2021; Artuğer 2024; Wang *et al.* 2020).

The Lorenz system has been widely investigated in the field of applied science and engineering. With the advent of the big data era, encrypted communication technology becomes more and more important (Ahuja *et al.* 2023; Can *et al.* 2023; Praveen *et al.* 2023). The building and optimization of a more secure block cipher system is essential. The excellent performance of the S-box is particularly important for the block cipher system. Different methods and principles can be used to encrypt information (Zied and Ibrahim 2023; Baowidan *et al.* 2024; Ali *et al.* 2022b). Chaotic systems are particularly important in the field of information security, and the construction of secure and robust S-boxes is of paramount significance to the building of block ciphers. The performance of the Henon map can also be more excellent. The method can be used to quickly search for the best S-box. This will help resolve a long-standing complex problem of the S-box (Mahboob *et al.* 2022; Zahid *et al.* 2023b; Kuznetsov *et al.* 2024; Mishra *et al.* 2023).

RELATED WORK

Significant research attention has been devoted to the use of chaotic systems in cryptographic algorithms. One proposed algorithm utilized bit permutation and phase encoding for image encryption. Another algorithm was based on a super Henon map and iteratively generated key components such as permutation bits, discrete chaotic system sequences, ciphering bits, private key, and auxiliary value (Fang *et al.* 2023; El-Latif *et al.* 2022; Muthu and Murali 2021; Zhang *et al.* 2023; Maazouz *et al.* 2022). A unified framework and general formula for an efficient chaotic encryption algorithm with non-volatile or based chaotic ciphers were also put forward. Additionally, an entropy analysis of chaotic encryption algorithms provided statistical information for security evaluation. Finally, a reversible chaos-based encryption algorithm introduced a public key to synchronize the permutation and ciphering behavior (Man *et al.* 2024; Dua *et al.* 2022; Umar *et al.* 2024; Pourasad *et al.* 2021; Li 2024; Kaur *et al.* 2020).

A new method for collecting specific initial conditions of the Henon map was introduced, along with a multi-layer image cryptosystem based on chaos. The complexity of an image encryption algorithm using the Rossler, Lorenz, and Fractional Order Lorenz System was assessed, revealing that the key-dependent measure was practical and effective (Niu *et al.* 2024; Galias 2022; Asbroek 2023; Wu *et al.* 2024; de Hénon 2024; Hareendran *et al.* 2024; Pal and Bhattacharjee 2020; Rong *et al.* 2022; Lenci *et al.* 2024). Additionally, a symmetric cryptosystem utilizing chaotic mapping and recurrent substitution boxes was discussed, along with a novel measure to evaluate the randomness of a repeated dynamic sequence. Furthermore, a design for S-boxes using a clonal selection algorithm and crossover immune cryptosystem was proposed, incorporating memory chaotic cryptography for optimization (Ahmad *et al.* 2022; Khaja and Ahmad 2023; Zhao *et al.* 2023; Abdulrazaq 2024; Alkhateeb and Al-Khatib 2020). Finally, an image encryption algorithm using a centralized chaotic map synthesized from the logistic map and a one-dimensional piecewise linear chaotic map with cross-mapping was presented (Nejatbakhsh 2022).

PROPOSED MODEL AND USED CHAOTIC MAPS

S-Boxes are critical components of the non-linear models used in block cipher systems, ensuring the confusion property a process that obscures the relationship between plaintext and ciphertext, enhancing security (Mohamed *et al.* 2014; Shannon 1949). For an S-Box to be effective, it must exhibit high levels of non-linearity and differentiability. S-Box designs can be broadly classified into two categories: static and dynamic. Static S-Boxes, used in earlier cipher systems, are more predictable and vulnerable to attacks, as their structure remains fixed throughout the encryption process. This vulnerability has led to the development of dynamic S-Boxes, which are key-independent and provide stronger security by continuously changing, making them harder for attackers to predict or exploit.

Chaos theory has been widely applied in communication systems due to its inherent randomness, making it useful for various applications, such as voice masking (Abdullah *et al.* 2022), noise reduction (Abdullah *et al.* 2015), frequency hopping (Ayoub *et al.* 2024), and image encryption (Salih *et al.* 2024). This work introduces a novel, dynamic S-Box design based on multi-dimensional chaotic maps, aiming to achieve high security performance and improve the robustness of modern cryptographic systems.

Henon map system is a one of the most two dimensional unpredictable chaotic maps, illustrate in equations (1,2); a,b are given as the control parameters with two initial conditions x_0, y_0:

$$x(n+1) = 1 + a(x(n))^2 + y(n) \tag{1}$$

$$y(n+1) = bx(n) \tag{2}$$

Lorenz Map System is a three dimensional chaotic map system, illustrate in equations (3 - 5) with three control parameters a,b,c and initial conditions x_0, y_0, z_0:

$$x(n+1) = a(y(n) - x(n)) \tag{3}$$

$$y(n+1) = x(n)(b - z(n)) - y(n) \tag{4}$$

$$z(n+1) = x(n)y(n) - (cz(n)) \tag{5}$$

PROPOSED SUBSTITUTION BOX (S-BOX)

Several methods employed to develop strong S-Box, the recent research based on mathematic calculation of chaotic behavior. This section presents novel strong dynamic S-Box with combing Henon and Lorenz chaotic maps. the proposed S-Box represented as 16 × 16 array with 8 bit for each element ranged from 0 to 255 providing of 256! probabilities. If one bit of the keys change cause the entire change. The procedure for generating S-Box explained in Figure 1 below.

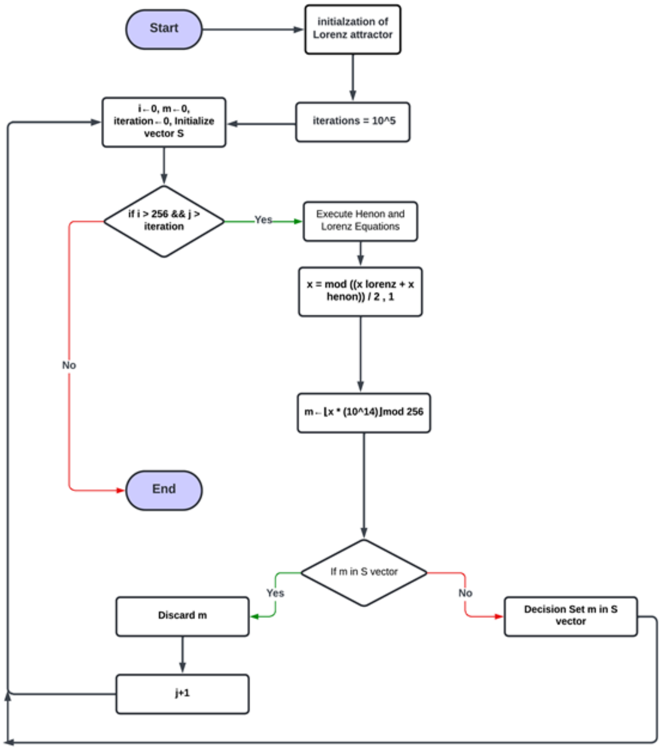

Figure 1 Flowchart of generating the proposed S-Box

S-Box Example

A complete example of a dynamic S-Box: assume $x_0 = 0.1$, $y_0 = 0$, $z_0 = 0$, $a = 10$, $b = 28$, $c = 8/3$, iterations = 100000, construction 16 × 16 S-Box with 8 bits size for each element, the elements are not repeated and random see Table 1.

Table 1 Generated S-Box using the proposed model

i/j	1	2	3	4	5	6	7	8	9	10	11	12	13	14	15	16
1	0	211	67	126	207	138	182	156	251	136	152	204	155	164	111	187
2	255	228	1	210	97	108	88	31	103	66	18	147	16	222	131	134
3	2	79	245	247	109	253	4	159	248	23	153	179	176	139	225	175
4	242	209	85	68	3	37	5	40	93	112	189	105	61	81	180	46
5	205	59	100	20	198	90	213	52	128	201	73	217	49	63	158	141
6	135	71	94	191	72	11	116	82	216	56	171	14	29	254	199	36
7	47	129	25	87	224	214	208	186	96	86	197	174	32	75	188	177
8	166	183	238	167	229	77	140	130	252	70	50	60	148	65	27	84
9	200	22	123	95	178	226	146	30	250	12	190	143	133	218	54	42
10	58	151	241	19	34	196	7	236	160	33	235	119	192	24	227	57
11	26	212	234	223	202	6	240	51	17	244	230	243	181	165	249	106
12	53	170	149	110	21	48	163	114	107	142	169	124	215	41	39	239
13	232	80	122	13	28	161	43	219	127	125	237	150	98	69	203	83
14	184	206	173	104	144	154	113	145	220	172	55	89	8	233	74	62
15	10	78	118	246	45	168	64	231	76	221	15	99	185	117	101	162
16	120	91	193	157	132	35	44	9	102	121	137	195	38	194	115	92

RESULTS AND DISCUSSION

This section presented cryptographic analysis of proposed S-Box security performance in Tables 2-5.

S-Box Performance analysis

Non-linearity: To reduce the possibility of linear cryptanalysis attacks and keeps the plaintext confidentiality there is a high need for ensure the non-linearity property of S-Box. The non-linearity of an n-bit S-Box can be calculated using equation 6,

$$\mathrm{NL}(b) = \frac{1}{2}\left[2^n - \max_{h\in\{0,1\}^n} |WS_b(h)|\right] \tag{6}$$

The walsh spectrum of a function can be computed by the equation 7,

$$WS_{b(h)} = \sum_{x\in\{0,1\}^n} (-1)^{b(x)\oplus(h\cdot x)} \tag{7}$$

Where $h \in \{0,1\}^n$ and $h.x$ is the dot product of h and x computed by equation 8,

$$h \cdot x = (h_1 \oplus x_1) + ... + (h_n \oplus x_n) \tag{8}$$

The non-linearity degree can be calculated by computing its Walsh spectrum and that will be necessary for high performance S-Box for cryptography application. The proposed S-Box has the following non-linearly values with a minimum value of 112 , maximum value of 128 and average value of 125.125 shown in Table 2.

Strict-Avalanche Criterion (SAC): If an S-box's SAC value is close to 0.5 that will be considered to have sufficient randomness. Table 3 shows the mean SAC value is 0.5097, the maximum value is 0.609 and the minimum value is 0.394, and that value make the proposed S-Box satisfying for high performance.

Table 2 Non-Linearity Values of Boolean Functions of the Proposed S-Box

Boolean Function	Non-Linearity (NL)
f_1	128
f_2	120
f_3	128
f_4	120
f_5	122
f_6	126
f_7	122
f_8	112
f_9	128
f_{10}	128
f_{11}	128
f_{12}	128
f_{13}	128
f_{14}	128
f_{15}	128
f_{16}	128

Table 3 SAC Values of the Proposed S-Box

i/j	1	2	3	4	5	6	7	8
1	0.4844	0.5000	0.4844	0.5781	0.4531	0.5781	0.5312	0.5312
2	0.5312	0.5000	0.5469	0.4844	0.4844	0.4688	0.5156	0.5312
3	0.4688	0.4531	0.5469	0.6094	0.5625	0.4688	0.5469	0.5000
4	0.4844	0.5625	0.5156	0.4531	0.5156	0.5312	0.4688	0.4219
5	0.4844	0.5625	0.4844	0.4219	0.5938	0.5312	0.5469	0.5625
6	0.5312	0.4531	0.4844	0.5469	0.5469	0.5312	0.5312	0.5000
7	0.5000	0.5156	0.5312	0.5938	0.5625	0.4219	0.5000	0.5781
8	0.5000	0.5000	0.4844	0.3594	0.4062	0.5469	0.4219	0.5781

Bit-Independence Criterion (BIC)

The security of S-Box will be successful if changing one bit of its input cause changing m bits of its output. For satisfying BIC performance, the equation $((Si(x)xorSj(z)) - (Si(x)xorSj((x)))$ for all inputs of x where x, z changed by only one bit. If the average of all values is close to 0.5 it can be said that S-Box operates well in terms of BIC conditions. Table 4 shows the values of BIC for non-linearity, the average 0.503, maximum and minimum are 0.609 and 0.375 respectively, these values showed weak connection between output bits satisfying BIC property.

Table 4 BIC Values Output for SAC of the Proposed S-Box

0.4688	0.5625	0.5156	0.5156	0.5000	0.5000	0.5000	0.5781
0.4531	0.4844	0.5000	0.5000	0.5469	0.5781	0.4062	0.4688
0.5625	0.3906	0.4688	0.5469	0.5000	0.5156	0.5000	0.5000
0.5469	0.5156	0.5000	0.5312	0.5156	0.4688	0.5156	0.5156
0.5156	0.4844	0.5469	0.4531	0.4219	0.4844	0.5156	0.4844
0.5000	0.5156	0.4688	0.4688	0.5312	0.5469	0.5312	0.5000
0.4844	0.3750	0.5156	0.5000	0.5312	0.5312	0.6094	0.4688
0.5156	0.4531	0.5312	0.4844	0.6094	0.5000	0.5156	0.4844

Linear-Probability (LP): Linear probability if a metric of correlation between S-Box inputs and outputs. The lower value of LP indicates high level cryptographic power. From equation 9 The maximum value of LP is 0.123 for the proposed S-Box is indicating good resistance against linear attacks.

$$LP = \max_{a_z, b_z \neq 0} \left| \frac{\#\{z \in \mathbb{N} \mid z \cdot a_z = S(z) \cdot b_z\}}{2^n} - \frac{1}{2} \right| \tag{9}$$

Differential-Probability (DP): Differential analysis is the technique of recovering the original plaintext from the encrypted ciphertext by differentiating each pairs of ciphertext from their corresponding plaintext. By this type of calculations the attacker can try to get the encryption key. The lower value of DP as shown in equation 10 indicates high level of security of cryptographic S-Box.

$$DP = \max_{\Delta_z \neq 0, \Delta_y} \left| \frac{\#\{z \in \mathbb{N} \mid S(z) \oplus S_{(z \oplus \Delta z)} = \Delta y\}}{2^n} \right| \tag{10}$$

The low differentiae is 0.0156 indicates the strength of the proposed S-Box.

Box Performance Comparison

Table 5 shows comparative study of the proposed work with other researchers in terms of performance metrics.

Table 5 Comparison of the Proposed Work with Other Studies

S-box Method	Min NL	Avg NL	Max NL	SAC	BIC	LP	DP
(Zahid *et al.* 2023a)	110	111.00	112	0.496	–	0.125	0.039
Proposed	112	125.25	128	0.509	0.503	0.123	0.015

S-box plays an important role in cryptographic operations. the proposed approach based on chaotic maps does not required calculating inverses or multiplicative mathematical operations which are complex and time consuming, the robustness was good according to performance metrics.

CONCLUSION

Information is a very important aspect in any corporation, it helps to make decision, that make the information transmission security is an essential for make profits. Cryptography is a security field that deals with information protection. This paper presents construction of strong cryptographically robust and dynamic S-box using compound chaotic maps. number of performance metrics such as non-linearity(NL), Strict Avalanche Criterion (SAC), Bit-Independence Criterion (BIC), Linear-Probability (LP) and differential-Probability (LP) for test the generated S-box and compared to recent researcher provide a satisfied strength recent cryptosystems. As a future work different hyperchaotic maps can be employed for build S_boxes enhancing cryptographic systems. Second approach is to employ this S_box for complete key generation, encryption and decryption to support overall security system performance.

Ethical standard

The authors have no relevant financial or non-financial interests to disclose.

Availability of data and material

Not applicable.

Conflicts of interest

The authors declare that there is no conflict of interest regarding the publication of this paper.

LITERATURE CITED

Abba, A., J. S. Teh, and M. Alawida, 2024 Towards accurate keyspace analysis of chaos-based image ciphers. Multimedia Tools and Applications .

Abdullah, H. N., S. S. Hreshee, and A. K. Jawad, 2015 Noise reduction of chaotic masking system using repetition method. Unpublished .

Abdullah, H. N., S. S. Hreshee, G. Karimi, and A. K. Jawad, 2022 Performance improvement of chaotic masking system using power control method. In *International Middle Eastern Simulation and Modelling Conference 2022, MESM 2022*, pp. 19–23.

Abdulrazaq, N. N., 2024 Generating of a dynamic and secure s-box for aes block cipher system based on modified hexadecimal playfair cipher. Zanco Journal of Pure and Applied Sciences **36**: 45–56.

Ahmad, A. D. Y., I. Hussain, M. Saleh, and M. T. Mustafa, 2022 A novel method to generate key-dependent s-boxes with identical algebraic properties. Journal of Information Security and Applications **65**: 103105.

Ahuja, B., R. Doriya, S. Salunke, and M. F. Hashmi, 2023 Hdiea: high dimensional color image encryption architecture using five-dimensional gauss-logistic and lorenz system. Connection Science **35**: 123–145.

Al-Dweik, A. Y., I. Hussain, M. Saleh, and M. T. Mustafa, 2022 A novel method to generate key-dependent s-boxes with identical algebraic properties. Journal of Information Security and Applications .

Al-Turjman, F. and H. Zahmatkesh, 2022 An overview of security and privacy in smart cities' iot communications. Transactions on Emerging Telecommunications Technologies **33**: e3677.

Ali, A., M. A. Khan, R. K. Ayyasamy, and M. Wasif, 2022a A novel systematic byte substitution method to design strong bijective substitution box (s-box) using piece-wise-linear chaotic map. PeerJ Computer Science .

Ali, R., J. Ali, P. Ping, and M. K. Jamil, 2024 A novel s-box generator using frobenius automorphism and its applications in image encryption. Nonlinear Dynamics .

Ali, R. S., O. Z. Akif, S. A. Jassim, A. K. Farhan, and E. S. M. El-Kenawy, 2022b Enhancement of the cast block algorithm based on novel s-box for image encryption. Sensors **22**: 5678.

Alkhateeb, F. and R. M. Al-Khatib, 2020 A survey for recent applications and variants of nature-inspired immune search algorithm. International Journal of Computational Intelligence Systems **13**: 1234–1248.

Alqahtani, J., M. Akram, G. A. Ali, N. Iqbal, and A. Alqahtani, 2023 Elevating network security: A novel s-box algorithm for robust data encryption. In *IEEE Conference on Network Security*, IEEE.

Alsaif, H., R. Guesmi, A. Kalghoum, and B. M. Alshammari, 2023 A novel strong s-box design using quantum crossover and chaotic boolean functions for symmetric cryptosystems. Symmetry **15**: 456.

Artuğer, F., 2024 Strong s-box construction approach based on josephus problem. Soft Computing **28**: 123–145.

Asbroek, T., 2023 The hénon map. Lecture notes or unpublished work, Available upon request.

Asghar, M. Z., S. A. Memon, and J. Hämäläinen, 2022 Evolution of wireless communication to 6g: Potential applications and research directions. Sustainability **14**: 6356.

Ayoub, H. G., Z. A. Abdulrazzaq, A. F. Fathil, S. A. Hasso, and A. T. Suhail, 2024 Unveiling robust security: Chaotic maps for frequency hopping implementation in fpga. Ain Shams Engineering Journal **15**: 103016.

Baowidan, S. A., A. Alamer, and M. Hassan, 2024 Group-action-based s-box generation technique for enhanced block cipher security and robust image encryption scheme. Symmetry **16**: 45.

Bavdekar, R., E. J. Chopde, A. Bhatia, and K. Tiwari, 2022 Post quantum cryptography: Techniques, challenges, standardization, and directions for future research. arXiv preprint arXiv .

Can, O., F. Thabit, A. O. Aljahdali, and S. Al-Homdy, 2023 A comprehensive literature of genetics cryptographic algorithms for data security in cloud computing. In *International Conference on Computing and Systems*, pp. 456–470, Taylor & Francis.

de Hénon, J. X., 2024 Hénon maps: a list of open problems. Arnold Mathematical Journal **10**: 45–60.

Dua, M., D. Makhija, P. Y. L. Manasa, and P. Mishra, 2022 3d chaotic map-cosine transformation based approach to video encryption and decryption. Open Computer Science **12**: 146–160.

Ekwueme, C. P., I. H. Adam, and A. Dwivedi, 2024 Lightweight cryptography for internet of things: A review. Endorsed Transactions on ... .

El-Latif, A. A. A., J. Ramadoss, B. Abd-El-Atty, and H. S. Khalifa, 2022 A novel chaos-based cryptography algorithm and its performance analysis. Mathematics **10**: 2736.

Fang, P., H. Liu, C. Wu, and M. Liu, 2023 A survey of image encryption algorithms based on chaotic system. The Visual Computer **39**: 2965–2983.

Farah, M. A. B., R. Guesmi, A. Kachouri, and M. Samet, 2020 A new design of cryptosystem based on s-box and chaotic permutation. Multimedia Tools and Applications **79**: 12345–12367.

Farooq, M. S., K. Munir, A. Alvi, and U. Omer, 2022 Design of a substitution box using a novel chaotic map and permutation. VFAST Transactions on Software .

Frank, E., 2024 Chaos theory, deterministic chaos, attractors, and sensitive initial conditions are key principles in chaotic encryption .

Galias, Z., 2022 Dynamics of the hénon map in the digital domain. IEEE Transactions on Circuits and Systems I: Regular Papers **69**: 1789–1800.

Gohar, Z. M. S., 2023 Securing engineering blueprints transmission using s-box and chaos theory .

Hareendran, A., B. V. Nair, S. S. Muni, and M. Lellep, 2024 Comparative analysis of predicting subsequent steps in hénon map. arXiv preprint arXiv:2403.xxxxx Preprint.

Hoseini, R., S. Behnia, S. Sarmady, and S. Fathizadeh, 2022 Construction of dynamical s-boxes based on image encryption approach. Soft Computing **26**: 12345–12360.

Hwang, J., G. Kale, P. P. Patel, and R. Vishwakarma, 2023 Machine learning in chaos-based encryption: Theory, implementations, and applications. In *IEEE Conference on Communications and Network Security*, IEEE.

Ilyas, B., S. M. Raouf, S. Abdelkader, and T. Camel, 2022 An efficient and reliable chaos-based iot security core for udp/ip wireless communication. In *IEEE International Conference on Internet of Things*, IEEE.

Indumathi, A. and G. Sumathi, 2022 Construction of key-dependent s-box for secure cloud storage. Intelligent Automation & Soft Computing .

Kaur, M., D. Singh, K. Sun, and U. Rawat, 2020 Color image encryption using non-dominated sorting genetic algorithm with local chaotic search based 5d chaotic map. Future Generation Computer Systems **107**: 333–350.

Khaja, I. A. and M. Ahmad, 2023 Similarity learning and genetic algorithm based novel s-box optimization. In *International Sym-*

posium on Intelligent Informatics, pp. 456–470, Springer.

Khoshafa, M. H., O. Maraqa, J. M. Moualeu, S. Aboagye, T. M. N. Ngatched, *et al.*, 2024 Ris-assisted physical layer security in emerging rf and optical wireless communication systems: A comprehensive survey. IEEE Communications Surveys & Tutorials Accepted for publication.

Knežević, K., 2023 Machine learning and evolutionary computation in design and analysis of symmetric key cryptographic algorithms. Preprint or unpublished report.

Kuznetsov, A., S. Kandii, E. Frontoni, and N. Poluyanenko, 2024 Sbgen: A high-performance library for rapid generation of cryptographic s-boxes. SoftwareX **25**: 101595.

Lenci, S., K. C. B. Benedetti, and G. Rega, 2024 Stochastic basins of attraction for uncertain initial conditions. Journal of Sound and Vibration **568**: 118028.

Li, L., 2024 A novel chaotic map application in image encryption algorithm. Expert Systems with Applications **238**: 121932.

Long, M. and L. Wang, 2021 S-box design based on discrete chaotic map and improved artificial bee colony algorithm. IEEE Access **9**: 123456–123467.

Maazouz, M., A. Toubal, B. Bengherbia, and O. Houhou, 2022 Fpga implementation of a chaos-based image encryption algorithm. Journal of King Saud University-Computer and Information Sciences **34**: 6114–6125.

Mahboob, A., M. Asif, M. Nadeem, and A. Saleem, 2022 A cryptographic scheme for construction of substitution boxes using quantic fractional transformation. In *IEEE International Conference on Cryptography*, pp. 123–128, IEEE.

Mahboob, A., M. Nadeem, and M. W. Rasheed, 2023 A study of text-theoretical approach to s-box construction with image encryption applications. Scientific Reports .

Man, Z., J. Li, X. Di, Y. Sheng, *et al.*, 2024 Double image encryption algorithm based on neural network and chaos. Chaos, Solitons & Fractals **178**: 114328.

Manzoor, A., A. H. Zahid, and M. T. Hassan, 2022 A new dynamic substitution box for data security using an innovative chaotic map. IEEE Access **10**: 98765–98780.

Mishra, R., M. Okade, and K. Mahapatra, 2023 Novel substitution box architectural synthesis for lightweight block ciphers. IEEE Embedded Systems Letters **15**: 65–68.

Mohamed, K., M. N. M. Pauzi, F. H. H. M. Ali, S. Ariffin, and N. H. N. Zulkipli, 2014 Study of s-box properties in block cipher. In *2014 International Conference on Computer, Communications, and Control Technology (I4CT)*, pp. 362–366, IEEE.

Muthu, J. S. and P. Murali, 2021 Review of chaos detection techniques performed on chaotic maps and systems in image encryption. SN Computer Science **2**: 386.

Naseer, M., S. Tariq, N. Riaz, and N. Ahmed, 2024 S-box security analysis of nist lightweight cryptography candidates: A critical empirical study. arXiv preprint arXiv Preprint.

Nejatbakhsh, A., 2022 *Scalable Tools for Information Extraction and Causal Modeling of Neural Data*. Columbia University.

Niu, S., R. Xue, and C. Ding, 2024 A dual image encryption method based on improved hénon mapping and improved logistic mapping. Multimedia Tools and Applications **83**: 12345–12367.

Pal, A. and J. K. Bhattacharjee, 2020 The hidden variable in the dynamics of transmission of covid-19: A hénon map approach. medRxiv Preprint.

Picek, S. and D. Jakobovic, 2022 Evolutionary computation and machine learning in security. In *Proceedings of the Genetic and Evolutionary*.

Pourasad, Y., R. Ranjbarzadeh, and A. Mardani, 2021 A new algorithm for digital image encryption based on chaos theory. Entropy **23**: 341.

Praveen, S. P., V. S. Suntharam, and S. Ravi, 2023 A novel dual confusion and diffusion approach for grey image encryption using multiple chaotic maps. Computer Science **14**: 789–801.

Progonatı, E., 2023 Chaos theory and political sciences. Diplomasi Araştırmaları Dergisi .

Rahman, A., K. Hasan, D. Kundu, and M. J. Islam, 2023 On the icn-iot with federated learning integration of communication: Concepts, security-privacy issues, applications, and future perspectives. Future Generation Computer Systems **136**: 1–15.

Rahman, Z., X. Yi, M. Billah, M. Sumi, *et al.*, 2022 Enhancing aes using chaos and logistic map-based key generation technique for securing iot-based smart home. Electronics .

Razaq, A., G. Alhamzi, S. Abbas, M. Ahmad, *et al.*, 2023 Secure communication through reliable s-box design: A proposed approach using coset graphs and matrix operations. Heliyon .

Rong, K., H. Bao, H. Li, Z. Hua, *et al.*, 2022 Memristive hénon map with hidden neimark-sacker bifurcations. Nonlinear Dynamics **108**: 1789–1805.

Salih, A. A., Z. A. Abdulrazaq, and H. G. Ayoub, 2024 Design and enhancing security performance of image cryptography system based on fixed point chaotic maps stream ciphers in fpga. Baghdad Science Journal **21**: 1754–1754.

Shannon, C. E., 1949 Communication theory of secrecy systems. The Bell system technical journal **28**: 656–715.

Sirohi, D., N. Kumar, P. S. Rana, S. Tanwar, and R. Iqbal, 2023 Federated learning for 6g-enabled secure communication systems: a comprehensive survey. Artificial Intelligence Review **56**: 1–34.

Umar, T., M. Nadeem, and F. Anwer, 2024 Chaos based image encryption scheme to secure sensitive multimedia content in cloud storage. Expert Systems with Applications **238**: 121656.

Waheed, A., F. Subhan, M. M. Suud, and M. Alam, 2023 An analytical review of current s-box design methodologies, performance evaluation criteria, and major challenges. Multimedia Tools and Applications .

Wang, J., Y. Zhu, C. Zhou, and Z. Qi, 2020 Construction method and performance analysis of chaotic s-box based on a memorable simulated annealing algorithm. Symmetry **12**: 788.

Wu, Y., S. Chu, H. Bao, D. Wang, *et al.*, 2024 Optimization of image encryption algorithm based on hénon mapping and arnold transformation of chaotic systems. IEEE Access **12**: 12345–12356.

Xun, P., Z. Chai, Z. Ma, L. Miao, and S. Li, 2024 Substitution box design based on improved sine cosine algorithm. In *Proceedings of the International*.

Ye, J. and Y. Chen, 2024 Sc-sa: Byte-oriented lightweight stream ciphers based on s-box substitution. Symmetry .

Zahid, A. H., M. J. Arshad, M. Ahmad, N. F. Soliman, and W. El-Shafai, 2023a Dynamic s-box generation using novel chaotic map with nonlinearity tweaking. Computers, Materials & Continua **75**.

Zahid, A. H., H. A. M. Elahi, M. Ahmad, and R. S. A. Said, 2023b Secure key-based substitution-boxes design using systematic search for high nonlinearity. In *IEEE Symposium on Security and Privacy*, pp. 456–461, IEEE.

Zelinka, I. and R. Senkerik, 2023 Chaotic attractors of discrete dynamical systems used in the core of evolutionary algorithms: state of art and perspectives. Journal of Difference Equations and Applications .

Zhang, H., H. Hu, and W. Ding, 2023 Image encryption algorithm based on hilbert sorting vector and new spatiotemporal chaotic system. Optics & Laser Technology **158**: 108859.

Zhao, M., H. Liu, and Y. Niu, 2023 Batch generating keyed strong s-boxes with high nonlinearity using 2d hyper chaotic map. Integration **90**: 123–135.

Zied, H. S. and A. G. A. Ibrahim, 2023 S-box modification for the block cipher algorithms. Przeglad Elektrotechniczny **99**: 123–128.

How to cite this article: Abdulrazaq, Z. A., Ayoub, H. G., and Ayoub, H. Synergistic Construction of High-Performance S-Boxes Based on Chaotic Systems: A Paradigm Shift in Cryptographic Security Design. *Chaos and Fractals*, 2(2), 43-49, 2025.

ADBA
Chaos and Fractals
Cutting-Edge Scientific Solutions

e-ISSN: 3023-8951
RESEARCH ARTICLE
Vol.2 / **No.**2 / 2025 / **pp.**50-58
https://doi.org/10.69882/adba.chf.2025074

Partial Prey Migration as a Non-autonomous Harmonic Oscillator: Chaos-Order Transitions in a Forced Classical Lotka-Volterra Model

Safieddine Bouali[*,1]
[*] University of Sfax, Faculty of Economics and Management, Department of Economics, Airport Rd. 14, K 4, Tunisia.

ABSTRACT I investigate how partial prey migration cycles, analogous to a non-autonomous harmonic oscillator, force the classical Lotka-Volterra model and reshape predator-prey interactions. A 3D nonlinear system is introduced, into which the external forcing replicates the entry and exit of partial migrants from the ecosystem, devoid feedback loops. Numerical simulations reveal an elusive resilience contour of the species interplay under stationary migration cycles. Thus, quasi-periodic and chaotic fluctuations appear at a minimum migration magnitude, vanishing beyond a bifurcation-induced tipping point. However, resilient interactions surge in localized hotspots, i.e., narrow regions of phase space and forcing intensity. It is striking to note that the detected chaos exhibits a threefold complexity related to migration magnitude, initial conditions, and a functional response parameter, implying a basin of attraction intertwined at fractal boundaries. In contrast, the resilience non-monotonicity fades due to ascending cycles of partial prey migration involving recruitment of a cohort of migrants by its resident species. In this case, chaos is suppressed, leading to predictable oscillations and phase-locking. Even extreme predator-prey ratios (e.g., 10:1) do not endanger prey. Despite its parsimony, the framework offers a tractable prototype with broader ecological applicability for studying how exogenous forcings (e.g., climate-driven phenology), can alter ecosystems.

KEYWORDS
Non-autonomous oscillator
Classical Lotka-Volterra model
Partial migration-driven dynamics
Chaos-Order
Resilience

INTRODUCTION

Many resident wildlife species share their habitat seasonally with their migrating conspecifics, a phenomenon called partial migration (Kaitala *et al.* 1993; Chapman *et al.* 2011; Lundberg 2013; Hansen *et al.* 2019; Peller *et al.* 2022). However, the periodic grouping of residents and migrants of the same species, observed particularly for prey, intrigues ecologists (De Leenheer *et al.* 2017). A key question that has been the foci of much research is that of the existence of asymptotical stable predator-prey interactions under weak prey immigration (Tahara *et al.* 2018; Alebraheem 2021; Kangalgil and Isik 2022; Alebraheem *et al.* 2024). Nevertheless, the dual role of partial migration (*immigration and emigration*) has been largely overlooked.

Here, I investigate how periodic waves of partial prey migration, akin to oscillatory forcing, reshape predator-prey dynamics. First, I introduce a minimalist yet ecologically grounded, dynamical system based on the classical Lotka-Volterra model (Lotka 1925; Volterra 1926), explicitly designating the interacting prey and predators as resident species. Despite idealized assumptions (e.g., exponential prey growth), it offers unparalleled mathematical parsimony, considering only essential functional responses, thus avoiding being engulfed by confounding factors such as refuges, Allee effects, or density-dependence processes (De Leenheer *et al.* 2017). Consequently, the role of partial prey migration as a forcing term becomes clearly discernible. Second, I formulate migration waves determined by the fitness of partial migrants, in accordance with empirical ecological studies (Alerstam *et al.* 2007; Vergara *et al.* 2007; Briedis *et al.* 2018; Nussbaumer *et al.* 2021, 2022). Hence, for both immigration and emigration, the fastest and fittest individuals lead, followed by slower, less fit stragglers, producing a staggered and velocity-dependent migratory flow. With this in mind, I define a simple harmonic oscillator (Gottlieb and Pfeiffer

---

Manuscript received: 2 June 2025,
Revised: 21 July 2025,
Accepted: 21 July 2025.

[1] safieddine.bouali@fsegs.usf.tn (**Corresponding author**)

2013) as an *ansatz*, to capture the momentum of the entry/exit dynamics of partial migration cycle related to the targeted habitat zone. Finally, I propose a parsimonious heuristic framework that encompasses the Lotka-Volterra model for resident prey and predator species and an oscillator for partially migratory prey, in a non-autonomous 3D system (Ashwin *et al.* 2017), allowing a numerical exploration of how their interplay modulates ecosystem resilience (Holling 1973; Peterson *et al.* 1998; Scheffer *et al.* 2001; Doherty *et al.* 2000; Dakos *et al.* 2015).

However, to probe its limits of sustainability, I adopt a simple definition: species interactions are resilient if they resist, absorb, or readjust to disturbances without collapsing over a specified very long period; otherwise, they are not resilient or experience precarious resilience. Specifically, I investigate whether variation in the magnitude of a stationary partial migration cycle could trigger a regime shift, along with the expected early warning signals (Guttal and Jayaprakash 2008; Scheffer *et al.* 2009; Carpenter *et al.* 2011; Evers *et al.* 2024). Using basic numerical tools (e.g., phase portraits, Poincaré maps), I characterize the resulting regime spectrum. Furthermore, I search for hotspots, i.e., regions in phase space exhibiting resilient species interactions, while the ecological ecosystem is under extreme prey migration pressure. Indeed, I test whether certain initial abundances of resident species can prevent ecosystem collapse in such a case.

Simulations of scenarios in which a net cohort of migratory prey switches to a sedentary behavior at each cycle are also performed. Indeed, flexible strategies have been observed in a significant number of species, where individuals can adopt either migratory or sedentary behavior (Brodersen *et al.* 2014). Thus, I explore the dynamical regimes induced by such partial prey migration with increasing cyclical trends, replenishing resident species. These results will be contrasted to those obtained under a stationary migratory cycle, where immigrant and emigrated prey populations are balanced, viewed through the lens of ecosystem resilience.

The paper is organized as follows. Section II introduces the heuristic framework and the tractable system, with ecological and mathematical grounds. Section III numerically explores partial migration scenarios (stationary and ascending cycles) and their implications for species interactions and ecosystem resilience. Section IV presents concluding remarks.

THE HEURISTIC FRAMEWORK

Several theoretical frameworks can be applied to explore the interplay of partially migratory prey with already interacting resident prey and predator species, depending on the type of inter- and intra-specific functional responses and environmental complexities. For the sake of simplicity, I selected the pioneering classical Lotka-Volterra model for my study, forcing it via a non-autonomous elementary harmonic oscillator, analogous to partial migration.

The Classical Lotka-Volterra Model: “stylized facts” of the Resident Predator-Prey Interactions

The classical Lotka-Volterra model (CLV) selected overly simplistic functional responses and idealized assumptions, but it remains relevant to illustrate the “stylized facts” of predator-prey interactions. Hence, such “idealizations may be far from the truth, without being epistemically inadequate” (Elgin 2004), and it is therefore well-grounded that the CLV constitutes a building block of a heuristic framework. It also specifically describes interactions between resident species, although the terms “resident” and “sedentary” are not used in CLV-related studies unless otherwise stated. Indeed, Volterra had clearly expressed his intention: “let us suppose we have two species living in the same environment” (Volterra 1931). Written as a pair of first-order ordinary differential equations, the CLV incorporates parameters (Table 1) describing the interactions between species as follows:

$$\begin{cases} \dfrac{dx}{dt} = x(\alpha - \beta y) \\ \dfrac{dy}{dt} = -y(\varphi - \mu x) \end{cases} \tag{1}$$

where x(t), and y(t) are the population of prey and predator, respectively.

Table 1 The Parameters of the Classical Lotka-Volterra Model

Parameter	Description
α	Per capita birth rate of prey in the absence of predators
β	Rate of fatal encounters between predator and prey
φ	Intrinsic mortality rate of predators in the absence of prey
μ	Reproduction rate of predator per prey
$\gamma = \frac{\mu}{\beta}$	Rate of converting ingested prey biomass into predator offspring

The model has two solutions:

$$S_0(x,y) = (0,0) \quad \text{and}$$

$$S_1(x,y) = \left(\frac{\varphi}{\mu}, \frac{\alpha}{\beta}\right)$$

Linearization states that S_0 is a saddle point and S_1 behaves either as a center or as a spiral point. Excluding the trivial solution S_0, and under usual initial conditions of strictly positive populations, the prey and predator populations exhibit stable oscillations without converging to S_1, thus defining a limit-cycle in the phase portrait. These interactions are inherently resilient, as they do not lead to ecological collapse. For instance, with parameters $P_0(\alpha, \beta, \varphi, \mu) = (0.2, 0.6, 1, 0.3)$, the solutions are the origin and

$$S_1(x,y) = \left(\frac{10}{3}, \frac{1}{3}\right)$$

Figure 1 illustrates these fluctuations when the model is parameterized with P_0 and the initial condition $\mathrm{IC}_0(x_0, y_0) = (0.7, 0.3)$ differs from the two solutions.

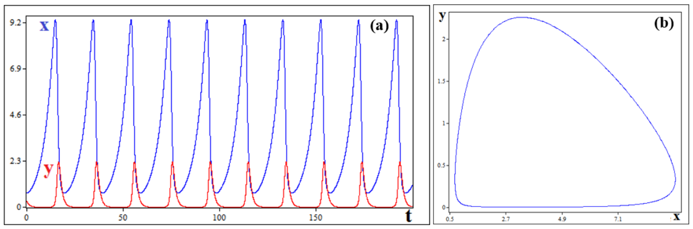

Figure 1 The Classical Lotka-Volterra prey-predator model. Parameters $P_0(\alpha, \beta, \varphi, \mu) = (0.2, 0.6, 1, 0.3)$ and initial condition $\mathrm{IC}_0(x_0, y_0) = (0.7, 0.3)$. (a) Time series of resident populations of prey x (blue line) and predator y (red line) up to t = 200, and (b) their limit-cycle in the phase portrait.

By considering these interactions as those of resident prey and predator species in an open ecosystem, I introduce the partial migration cycle of prey as an oscillatory mechanism.

A Non-autonomous Harmonic Oscillator as an Analogue of Partial Prey Migration

Inspired by empirical ecological studies, I propose a simplified non-autonomous harmonic oscillator that describes partial prey migration, where $x_m(t)$ represents the accumulation of migrants in the habitat area and $M(t)$ its velocity at time t:

$$\begin{cases} \frac{dx_m}{dt} = \lambda M \\ \frac{dM}{dt} = A\cos(\Omega t) \end{cases} \tag{2}$$

Table 2 The forcing parameters (all positive)

Parameter	Description
λ	Control parameter of the migration coupling
A	Amplitude of migration velocity
Ω	Forcing frequency

Technically, the velocity M is the derivative of the corresponding innate momentum, i.e. the increment/reduction of partial migrants within the ecosystem. Additionally, the cosine function governs the Hamiltonian flow, shaping the partial migration cycle of prey. Although it is easy to avoid such a non-autonomous velocity vector by introducing a third dependent variable, I keep time t as an explicit variable, with mathematical parsimony guiding this study. Thus, the Hamiltonian of this purely linear oscillator has the formulation:

$$H(x_m, M, t) = \frac{\lambda}{2}M^2(t) - A\cos(\Omega t)x_m$$

$H(x_m, M, t)$ represents the total energy of the oscillator, which is the sum of its kinetic energy and potential energy, respectively.

For $M = 0$, the Hamiltonian is not conserved due to time-dependent forcing, but conservative, which gives periodic orbits in the phase space (x_m, M). For values of M^+, it is also not conserved, but non-conservative with energy growth, exhibiting spirals with drift.

It follows that, in general cases, the exact solutions of (2) are:

$$x_m(t) = \lambda M_0(t) + \lambda\frac{A}{\Omega^2}(1 - \cos(\Omega t))M(t) = M_0 + \frac{A}{\Omega}\sin(\Omega t)$$

By setting $A = \Omega = 1$, and the initial condition $(x_m, M_0) = (0, 0)$, i.e., zero population of migrants, and a null increment at t_0, $x_m(t)$ varies sensitively with λ:

$$x_m(t) = \lambda(1 - \cos(t)), M(t) = \sin(t)$$

The series of regular migratory waves encapsulates the transient occupancy of the habitat area according to the stable period of these oscillations, regardless of the parameter λ. More precisely, the increment M varying in the interval [-1, 1] drives both facets of the cycle, i.e. immigration and emigration, by its positive and negative ranges respectively. First, strictly positive M values govern the entry of partial migrants in the habitat area in two steps. As M increases from 0 to 1, the number of immigrants rises at an increasing pace. Conversely, as M decreases from 1 to 0, it also rises, but at a decreasing pace, reaching zero. The immigrant population has thus reached its maximum level, marking the end of migratory entry into the ecosystem and thus the first facet of the cycle. Second, strictly negative M values govern the exit of partial migrants from the habitat area, also in two steps. When M varies from 0 to -1, and given its absolute value, the number of emigrants rises at an increasing velocity. On the other hand, when M varies from -1 to 0, and also given its absolute value, it rises but at a decreasing velocity until reaching zero. Thus, the withdrawal process is fully realized, signaling that all emigrants have left the ecosystem. With this second facet, the entire migratory cycle is completed (Figure 2).

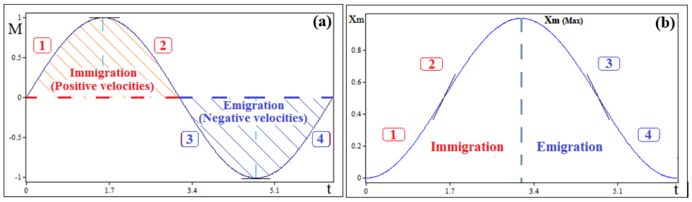

Figure 2 The M-velocity waveform shapes both facets of the migration cycle. Illustration with the initial condition $(x_m(0), M_0) = (0, 0)$ for the cycle n°1. a) Positive values of M drive the migrant population $x_m(t)$ into the ecosystem at an increasing (box 1) and then decreasing (box 2) pace. Conversely, negative values withdraw migrants xm(t) from the ecosystem at an increasing (box 3) and then decreasing (box 4) velocities given their absolute values. (b) Bell-curve of partial migrants $x_m(t)$ in the habitat area. After reaching its maximum number, the migration process reverses and all have left the ecosystem at the end of the cycle.

With momentum kept unchanged, with $M_0 = 0$ and A = Ω = 1 the partial migrant population increases significantly with magnitude λ. Indeed, for several values of λ $\epsilon \in$ {0.1, 0.2, 0.5, 0.7, 1}, the migratory cycle exhibits higher amplitudes (Figure 3a). Therefore, the phase portrait of the accumulation of partial migrants x_m as a function of the velocity M, with the corresponding λ value, exhibits periodic orbits. Figure 3b illustrates, for the selected set of λ, these cycles in phase space, where the (M, x_m) plot moves in counterclockwise orbits from the origin.

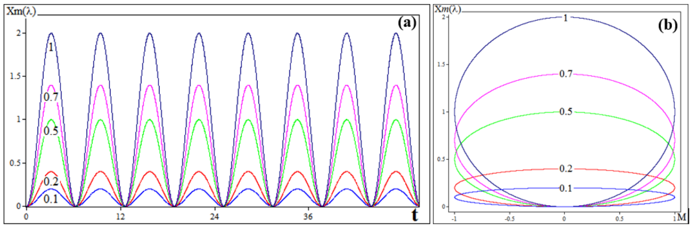

Figure 3 Partial prey migration cycles with A = Ω = 1, and the initial condition $(M_0, x_m(0)) = (0, 0)$ up to t = 50. (a) Accumulation of partial migrants x_m vs. time for selected values of the magnitude λ $\in$ {0.1, 0.2, 0.5, 0.7, 1}. (b) Their phase portraits where (M, x_m) plot rotates 2π counterclockwise from the origin to complete a partial migration cycle.

The Unified Model

Consider the non-autonomous 3D system where x(t) and y(t) are the abundances of prey and predators respectively, and M(t) the velocity/displacement of migratory prey within the ecosystem. It is formulated as follows:

$$\begin{cases} \frac{dx}{dt} = x\,(\alpha - \beta y) + \lambda M \\ \frac{dy}{dt} = -y\,(\varphi - \mu x) \\ \frac{dM}{dt} = A\cos(\Omega t) \end{cases} \tag{3}$$

where α, β, φ and μ, parameters identical to those of the CLV (see Table 1), and λ, A, and Ω, parameters of the forcing oscillator. (see Table 2). When $\lambda = 0$, the system is reduced to the unforced CLV, exhibiting neutral oscillations around an equilibrium. For $\lambda > 0$, prey migration driven by oscillatory forcing is enabled in the first equation by the term λM, where λ adapts its impact. From then on, the system becomes non-autonomous via $\cos(\Omega t)$ according to the mechanism introduced in the previous sub-section. For small λ, the system can be approximated using perturbation methods. I obtain:

$$\frac{dx}{dt} \approx x(\alpha - \beta y) + \lambda \frac{A}{\Omega}\sin(\Omega t)$$

, where

$$M(t) = M_0 + \frac{A}{\Omega}\sin(\Omega t)$$

As formulated in the first equation, the migrants avoid lethal encounters with predators upon entering the ecosystem and are therefore not affected by the parameter β. They are expected to be moving targets, more vigilant in their new environment, and it will inevitably be difficult for a predator to surprise them. Although studies have reported greater predation avoidance in partial migrants than in residents (Skov *et al.* 2013; Zúñiga *et al.* 2017; Berg *et al.* 2023), in the presented system, this immediate survival of migrants within the ecosystem is lost at the next step, i.e., the iteration at t+1. This cohort is then faced with a lethal encounter rate β and a predator conversion rate μ identical to those of resident prey, as indicated in the second equation. Regarding the third equation, technically, the forcing injects/removes prey periodically into the CLV without a feedback loop from its state variables. Therefore, the system no longer distinguishes between migratory prey and residents that interact together with the resident predator. In the following, I numerically simulate the non-autonomous three-dimensional ODE system in order to evaluate its resilience with the 4th-order Runge-Kutta method.

NUMERICAL RESULTS

To scrutinize the dynamical regimes of the system, predator-prey interactions are considered resilient if they persist until at least $t = 10^5$. Otherwise, they are not resilient if they collapse before $t = 10^4$, and resilience is precarious for $t \in [10^4, 10^5]$. In the first analysis, the magnitude λ serves as the control parameter for the stationary partial migration cycle. Specifically, λ is categorized as follows: low migration intensity for $0 < \lambda \leq 0.5$, moderate intensity for $0.5 < \lambda \leq 2$, and massive intensity for $\lambda > 2$. The second analysis examines partial prey migration cycles with a positive trend. All simulations use fixed parameters $A = \Omega = 1$.

Stationary Cycles of Partial Prey Migration Imply Elusive Ecosystem Resilience

By setting $M_0 = 0$, the partial prey migration adheres to a stationary cycle fully anchored in recurring dates, exhibiting identical waveform movements. Hence, the number of immigrants and emigrants must be roughly balanced. This constraint implies that losses of partial migrants due to predation within the ecosystem are compensated either by reproduction or by recruitment of a cohort of residents.

Figure 4 provides a direct comparison of partial migrating prey $X_m(\lambda)$ for selected λ magnitudes and resident prey abundance when the CLV and the partial prey migration oscillator are not yet connected. I find that a single cycle of resident prey-predator interactions encompasses three migration pulses, allowing us to explore the resilience limits of the system. Further studies should consider A and Ω as control parameters.

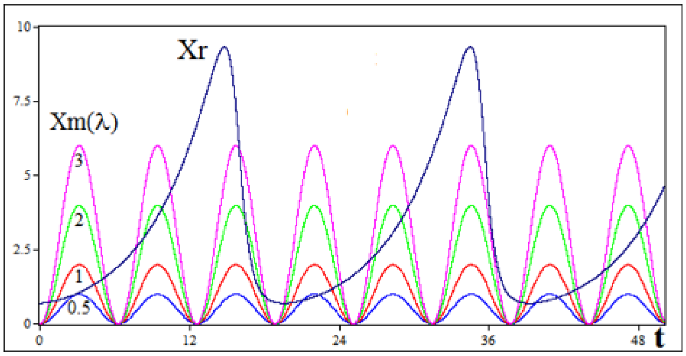

Figure 4 Accumulations of partially migratory prey $X_m(\lambda)$ for the magnitudes $\lambda \in \{0.5, 1, 2, 3\}$ and of resident prey X_r before forcing the CLV by the oscillator up to $t = 50$. CLV parameters $P_0(\alpha, \beta, \varphi, \mu) = (0.2, 0.6, 1, 0.3)$, and initial condition $IC_0(x_0, y_0) = (0.7, 0.3)$. Initial condition of the partial migration oscillator $(M_0, X_m(0)) = (0, 0)$.

Dependence on the magnitude parameter λ

In the first set of simulations, the weak coupling of the oscillator leads to immediate non-periodic fluctuations in species populations. As shown in Figure 5, for $\lambda = 0.1$ and 0.2, the time series of $x(t)$ and $y(t)$, and in particular the phase portraits of the state variables (x, y) suggest asymptotically unstable oscillations under parameters $P_0(\alpha, \beta, \varphi, \mu) = (0.2, 0.6, 1, 0.3)$ and the initial condition $IC_0(x_0, y_0, M_0) = (0.7, 0.3, 0)$.

Furthermore, the Poincaré sections, plotted when $M = 0$ (i.e., at the precise moments of the beginning and end of the partial migration cycles, as well as at the moments separating immigration and emigration), illustrate the complex trajectory of species populations.

These fluctuations persist resiliently for λ in the interval $]0, 0.22[$. However, a slight increase in coupling, i.e., a partial migration magnitude varying only by $\Delta\lambda = 0.01$, results in an almost immediate vanishing of predator-prey interactions, signaling a critical transition. Since the catastrophic event results from the continuous change in λ, the system has crossed a bifurcation-induced tipping point (or B-tipping).

Starting with the sudden and drastic change at the critical value $\lambda_c = 0.23$ and for slightly higher values, interactions exhibit volatile dynamics and therefore do not even reach the threshold of precarious resilience. For example, at $\lambda = 0.5$, species become extinct around $t \approx 170$ as shown in Figure 6. The upward alignment of the last four prey population peaks may suggest an early warning signal of impending ecosystem collapse.

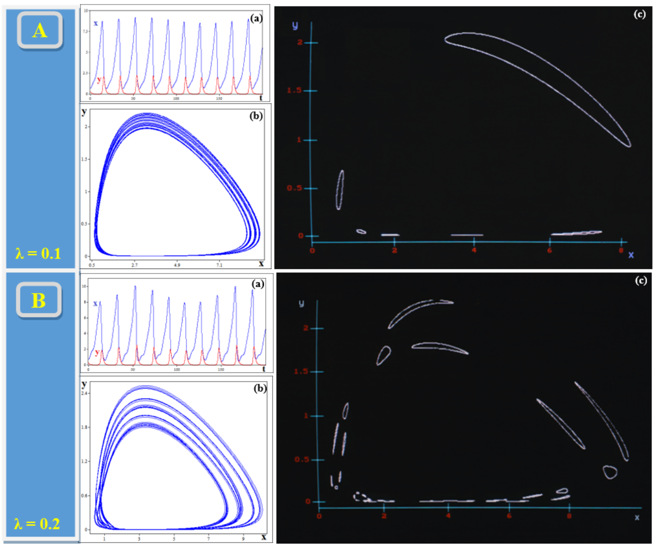

Figure 5 Numerical simulations with parameters $P_0(\alpha, \beta, \lambda, \varphi, \mu) = (0.2, 0.6, \lambda, 1, 0.3)$ and initial condition $IC_0(x_0, y_0, M_0) = (0.7, 0.3, 0)$. (a) Time series of x and y (prey and predator abundances respectively) first $t = 200$ (b) Phase portrait of state variables x and y (c) Poincaré maps ($M = 0$) Panel A: $\lambda = 0.1$. Panel B: $\lambda = 0.2$.

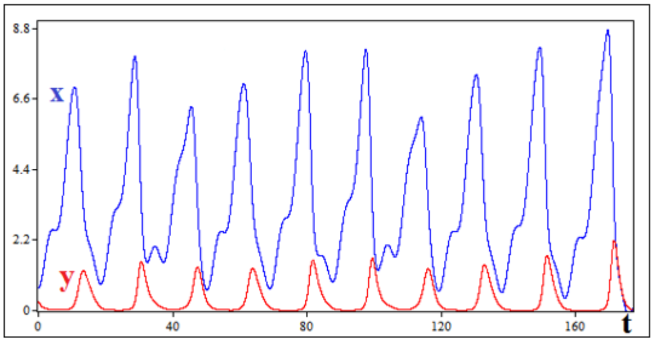

Figure 6 Time series of prey and predator accumulations, x and y respectively, for magnitude $\lambda = 0.5$ of partial prey migration. The collapse occurs at $t \approx 170$. Parameters $P_0(\alpha, \beta, \lambda, \varphi, \mu) = (0.2, 0.6, 0.5, 1, 0.3)$, and the initial condition $IC_0(x_0, y_0, M_0) = (0.7, 0.3, 0)$.

Surprisingly, resilient interactions are restored within very narrow windows of λ. These hotspots are scattered and detected in small numbers under the aforementioned parameters $P_0(\alpha, \beta, \varphi, \mu) = (0.2, 0.6, 1, 0.3)$, and the initial condition $IC_0(x_0, y_0, M_0) = (0.7, 0.3, 0)$. Figure 7 presents time series of prey and predator accumulations, x and y respectively, phase portraits and Poincaré maps ($M = 0$) for some of the identified magnitudes, e.g., $\lambda \in \{0.7, 1, 1.5\}$, which exhibit rare resilient interactions. Indeed, to avoid prey extinction and therefore predator starvation, a key condition to ensure ecosystem resilience must be met: $\lambda M(t) > x(\alpha - \beta y)$.

Dependence on initial conditions of the species populations and parameter α

The proposed system also exhibits extreme sensitivity to the initial sizes of resident species, as interactions can abruptly disappear even after small changes. Indeed, the resilient regimes shown in Figure 7 rapidly collapse when $IC_0(x_0, y_0, M_0) = (0.7, 0.3, 0)$ is adjusted to $IC_1(x_0, y_0, M_0) = (0.6, 0.2, 0)$, while the parameters remain unchanged. Conversely, the volatile dynamics illustrated in Figure 6 for $\lambda = 0.5$ becomes resilient when the initial conditions are slightly shifted from $IC_0(x_0, y_0, M_0) = (0.7, 0.3, 0)$ to $IC_2(x_0, y_0, M_0) = (0.9, 0.3, 0)$, as illustrated in Figure 8, panel A. It is also worth mentioning the significant dependence on prey birth rate, the parameter α. For example, the collapsed regime mentioned in Figure 6 becomes resilient when only the parameter α varies from 0.2 to 0.5 (Figure 8, Panel B).

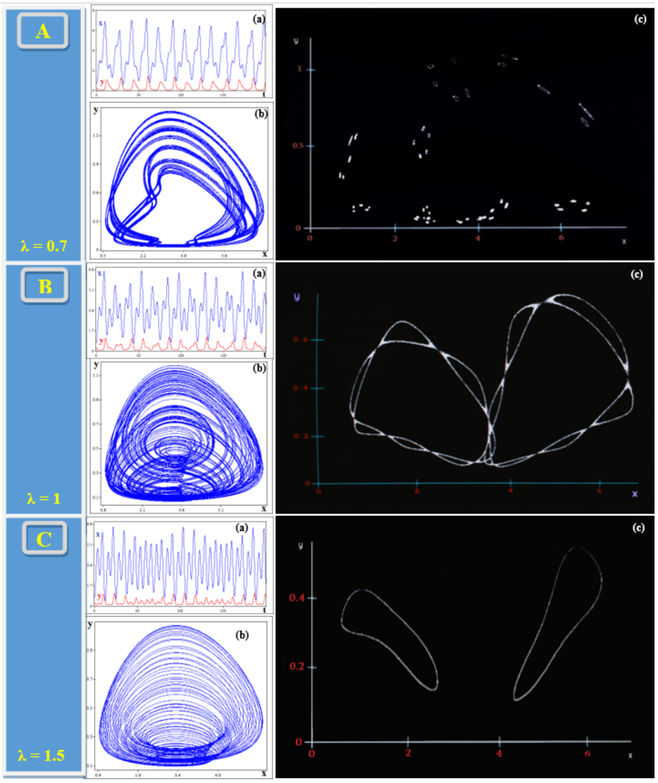

Figure 7 Hotspots of resilient quasi-periodic or chaotic dynamics in a very narrow window of magnitude λ. Numerical simulations with parameters $P_0(\alpha, \beta, \varphi, \mu) = (0.2, 0.6, 1, 0.3)$ and initial condition $IC_0(x_0, y_0, M_0) = (0.7, 0.3, 0)$. (a) Time series of x and y, the abundances of prey and predators, respectively, for the first 200 iterations. (b) Phase portrait of x and y. (c) Their Poincaré map ($M = 0$). Panel A: $\lambda = 0.7$, Panel B: $\lambda = 1$, Panel C: $\lambda = 1.5$

A threefold complexity of chaos

To characterize the chaotic nature of the system, the largest Lyapunov exponent (LLE) is computed. Thus, the detection of a single positive exponent among the three for a three-dimensional system confirms the signature of chaos. As shown in Figure 9, the LLE spectra computed for $\lambda \in [0, 1.7]$ and the same P_0 parameters, but under two distinct initial conditions, namely $IC_0(x_0, y_0, M_0) = (0.7, 0.3, 0)$ and $IC_1(x_0, y_0, M_0) = (0.9, 0.3, 0)$, state the hallmark of chaos.

Alongside this, the dissimilarity of LLE spectra provides compelling evidence of sensitive dependence on initial conditions. Furthermore, sawtooth-shaped spectra with steep peaks and dips are likely indicators of tipping points and thus express regime shifts (Nazarimehr *et al.* 2017), either in response to the variation of the parameter λ or to the initial conditions. The three dependencies of the system under λ, the initial conditions, and the

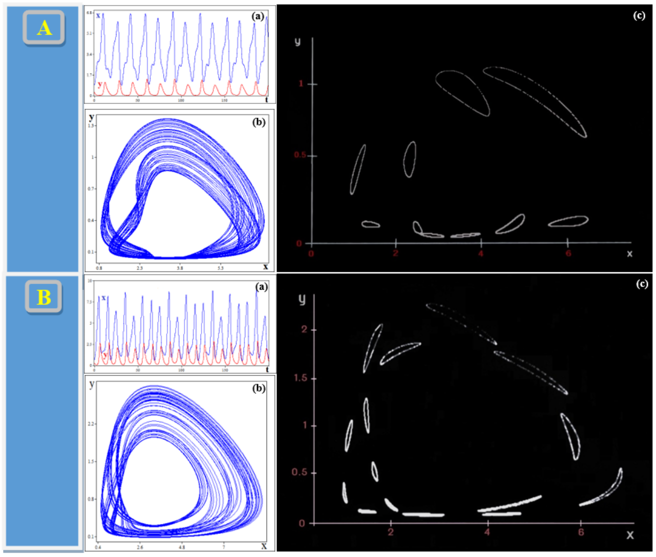

Figure 8 Sensitive dependencies on the initial sizes of species and the parameter α. (a) Time series of state variables x and y, the prey and predator populations, respectively; first $t = 200$, (b) the corresponding phase portrait, and (c) Poincaré map after transients died down. Panel A: Parameters $P_0(\alpha, \beta, \lambda, \varphi, \mu) = (0.2, 0.6, 0.5, 1, 0.3)$ and $IC_1(x_0, y_0, M_0) = (0.9, 0.3, 0)$. Compare with collapsed regime in Figure 6 with $IC_0(x_0, y_0, M_0) = (0.7, 0.3, 0)$. Panel B: Parameters $P_0(\alpha, \beta, \lambda, \varphi, \mu) = (0.5, 0.6, 0.5, 1, 0.3)$ and $IC_0(x_0, y_0, M_0) = (0.7, 0.3, 0)$. Compare with the same collapsed regime in Figure 6 where $\alpha = 0.2$.

functional response parameters α might be expected to entail an intertwined and highly entangled basin of attraction, delimited by fractal boundaries.

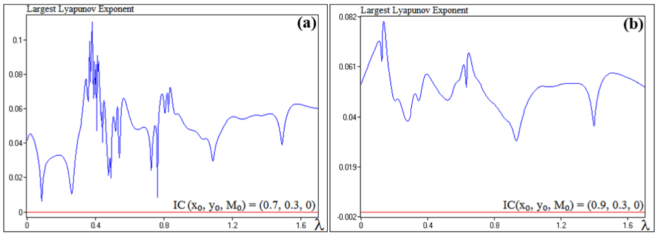

Figure 9 Largest Lyapunov exponent (LLE) spectra computed for migration magnitude λ varying in the range $[0, 1.7]$. $P_0(\alpha, \beta, \varphi, \mu) = (0.2, 0.6, 1, 0.3)$, and two distinct initial conditions. (a) LLE spectrum with $IC_0(x_0, y_0, M_0) = (0.7, 0.3, 0)$. (b) LLE spectrum recomputed with $IC_1(x_0, y_0, M_0) = (0.9, 0.3, 0)$.

Upward Cycles of Partial Prey Migration Preserve Ecosystem Resilience

In scenarios where M_0 has strictly positive values, and $\lambda = A = \Omega = 1$, partial prey migrations exhibit upward cycles. Thus, a number of partially migratory prey are recruited by its resident species in the habitat area during each cycle (Figure 10).

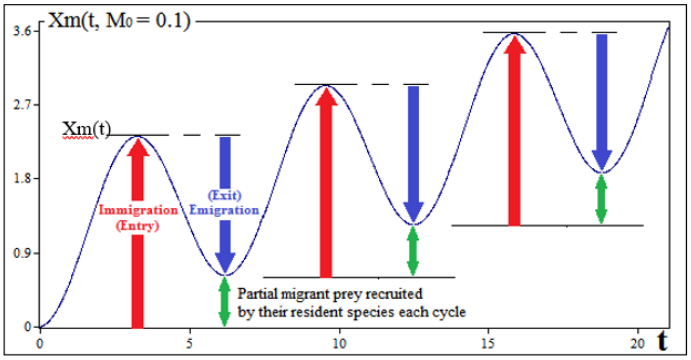

Figure 10 A net cohort of migrants settles in the ecosystem each cycle. Time series of partial prey migration up to $t \approx 22$. $\lambda = 1$ and initial condition Xm$(t, M_0) = (0, 0.1)$.

The velocity $M(t)$, or augmentation/reduction of migrants, varies in the range $[-1 + M_0, 1 + M_0]$, as shown for example in Figure 11a for several values of $M_0 \in \{0, 0.5, 1, 2\}$. Furthermore, Figure 11b illustrates the cycles of partial migrants $X_m(M_0)$ for the selected values of M_0 compared to the abundance of resident prey X_r, already interacting with the predator, before coupling. In the following, still with $\lambda = 1$ and considering M_0 as a control parameter, I examine how ascending cycles of partial prey migration shape overall ecosystem dynamics and thus its resilience. Here, the recruitment is considered low for $0 < M_0 \leq 0.2$, moderate for $0.2 < M_0 \leq 1$, and massive for higher values.

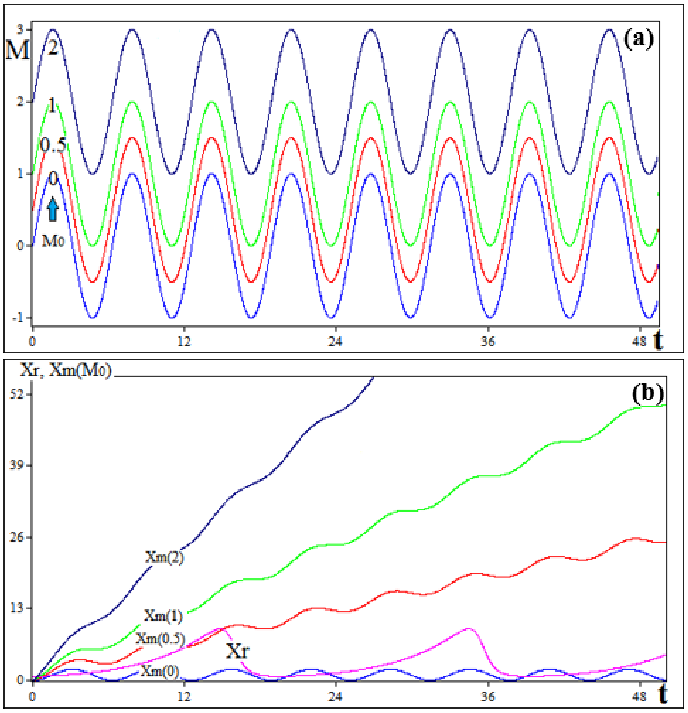

Figure 11 Upward cycles for several M_0 values and corresponding abundances of partial migratory prey. The migratory prey population is governed by a stationary cycle when $M_0 = 0$, and by upward cycles when $M_0 > 0$. Parameters: $\lambda = A = \Omega = 1$, and initial condition $(X_m, M_0) = (0, M_0)$, till $t = 50$. (a) $M(t)$ for $M_0 \in \{0, 0.5, 1, 2\}$, and (b) time series of $X_m(M_0)$ for the selected M_0 compared with the resident prey population X_r already interacting with predators, before coupling. Parameters $P_0(\alpha, \beta, \varphi, \mu) = (0.2, 0.6, 1, 0.3)$, and the initial condition $IC_0(x_0, y_0) = (0.7, 0.3)$.

Double-peaked fluctuations and phase-locking

Numerical computations reveal pronounced periodic double-peaked fluctuations in the prey population for $M_0 \in \{0.1, 0.2\}$, resulting in characteristic orbits in the phase portraits (Figure 12). This pattern is derived from the asynchrony between the waxing and waning of resident and partially migratory prey populations, associated to the recruitment of a cohort of migrants by the resident population each cycle. As M_0 increases from 0.1 to 0.2, both prey and predator populations show slow but steady growth, observed across the entire range of $M_0 \in [0, 0.2]$.

In the next, broader range of $M_0 \in [0.2, 1]$, and after transients died down, the populations of both species increase and maintain stable fluctuations, adopting regular wave patterns. These partial migration cycles with moderate recruitment introduce a significant stabilizing effect on intrinsic species interactions. Indeed, for M_0 equal to 0.5 and 1, phase portraits exhibit periodic orbits, confirming that newly settled migrants do not jeopardize the ecosystem resilience (Figure 13). More specifically, the time series reveal a characteristic phase locking, with the predator population peak lagging at approximately a quarter cycle (90°) compared to that of the prey. This type of asynchronous fluctuations is consistent with the literature on in-phase, anti-phase, and phase-locking synchronizations in coupled-species oscillators (Winfree 1967; Vandermeer 2006; Vasseur and Fox 2009; Smirnov and Pikovsky 2024).

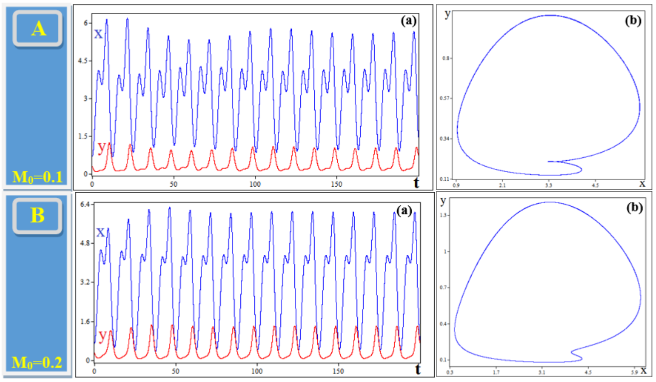

Figure 12 Double-peaked prey and predator populations with low recruitment. Dynamical regimes with weak ascending cycles of the partial migration. $P_0(\alpha, \beta, \lambda, \varphi, \mu) = (0.2, 0.6, 1, 1, 0.3)$ and initial condition $(x_0, y_0, M_0) = (0.7, 0.3, M_0)$. (a) Time series of the prey and predator populations up to $t = 200$, and (b) their phase portraits after transients died down. Panel A: $M_0 = 0.1$. Panel B: $M_0 = 0.2$.

"Catching up" and overtaking game for massive recruitment

The partial migration of prey exhibiting extreme upward cycles stabilizes, as in the previous cases, the species populations and induces limit cycles (Figure 14). It is noteworthy that a "catching up" process between the prey and predator populations occurs, balancing them at $M_0 = 6.05$.

The predator species experiences a phenomenal increase in abundance due to the recurrent and strong recruitment of immigrant prey, via the conversion rate of ingested prey into predatory offspring. This process, observed for example at the invasive level of $M_0 = 80$, leads to a predator population exceeding tenfold that of the prey. Although this ratio may suggest that the resident prey is an endangered species, the settlement of partially migratory prey replenishes the residents each cycle and thus prevents their extinction.

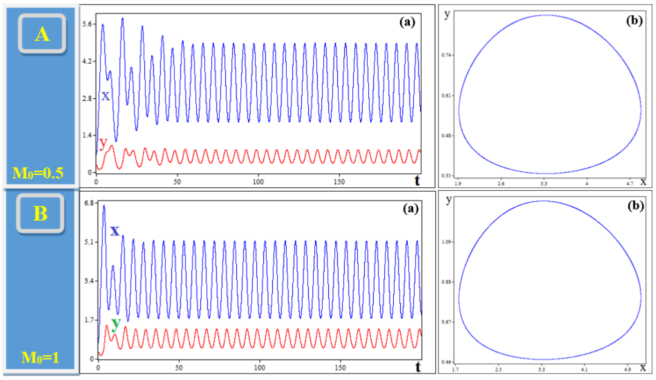

Figure 13 Phase locking of predator and prey populations by approx. one-quarter cycle (90°) for moderate recruitment. Parameters $P_0(\alpha, \beta, \lambda, \varphi, \mu) = (0.2, 0.6, 1, 1, 0.3)$ and the initial condition $(x_0, y_0, M_0) = (0.7, 0.3, M_0)$. (a) Time series of prey and predator populations up to $t = 200$, and (b) their limit cycle in phase space. Panel A: $M_0 = 0.5$. Panel B: $M_0 = 1$.

This result is consistent with the seminal contribution of Levins (1969), and the source-sink habitats of the metapopulation approach (Holt 1985; Hanski 1999; Taylor and Hall 2012). Indeed, Pulliam (1988) notes that in sink areas: "the population may persist in such habitats, being locally maintained by continued immigration from more productive 'source' areas nearby." Here, no discontinuity in ecosystem resilience is detected for $M_0 > 0$ of partial prey migration cycles since the domain of attraction envelops the entire phase space.

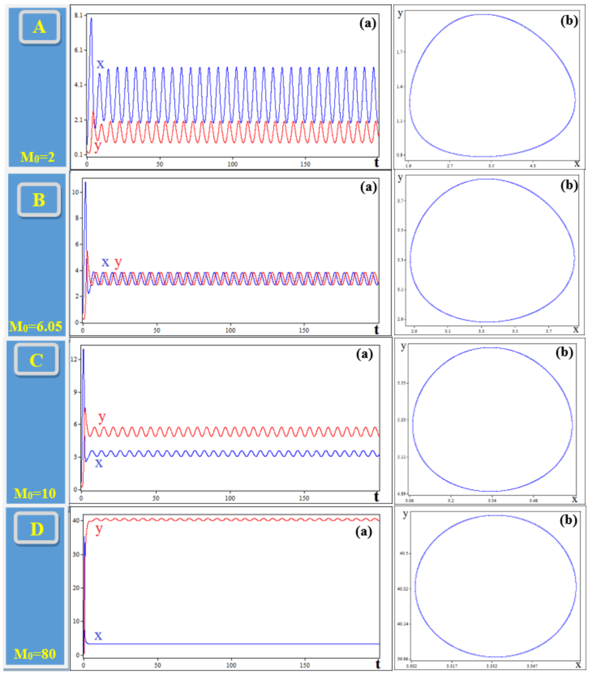

Figure 14 The predator population approaches, catches up with, and then overtakes the prey population. Parameters $P_0(\alpha, \beta, \lambda, \varphi, \mu) = (0.2, 0.6, 1, 1, 0.3)$ and initial condition $(x_0, y_0, M_0) = (0.7, 0.3, M_0)$. (a) Time series of prey and predator populations up to $t = 200$, and (b) associated limit cycle in the phase space after transients died down. Panel A: $M_0 = 2$. Panel B: $M_0 = 6.05$. Panel C: $M_0 = 10$. Panel D: $M_0 = 80$.

CONCLUSION

In this study, I focused on the magnitude and trend of the cycle, two key dimensions of partial prey migration, conceptualized as an oscillatory mechanism. Thus, the proposed system uncovered a striking dichotomy: partial migration acts as a *dual* driver of chaos and order in open ecological ecosystems. Hence, even a low magnitude of stationary migratory cycles inject critical instability into predator-prey interactions, fostering resilient chaos that persists until the migration magnitude crosses a bifurcation-induced threshold. Beyond this B-tipping, collapse ensues, yet chaos resurges in localized hotspots, suggesting fractal basin boundaries and a non-monotonic dependence on magnitude, initial conditions and α parameter.

Such behavior mirrors the sensitive dependence of driven oscillators, where minute parameter shifts precipitate phase transitions. Conversely, upward-trending cycles suppress the risk of ecosystem collapse, stabilizing interactions in predictable limit cycles even leading to phase synchronizations. This chaos-to-order transition challenges conventional views on the destabilizing role of immigration, positioning flexible migratory behavior as a key ecological parameter. Indeed, the route from chaotic regimes, ecosystem extinction, and elusive resilience to the realm of order is simply unlocked when the trend in partial prey migration cycles becomes strictly positive, even slightly. This dichotomy echoes a critical phenomenon in oscillatory systems, where the sign of the trend (positive or neutral) determines whether dynamics converge toward equilibrium or diverge into turbulence.

Mainly, I acknowledge deliberate simplifications of the introduced heuristic framework, such as multiple waves of partial migration for a single predator-prey interaction cycle. It nevertheless provides a preliminary and tractable prototype for a valuable approximation of how exogenous pulses trigger bifurcation-like behaviors (e.g., climate-induced phenological changes). Framing migration as a forced oscillator underscores its capacity to reconfigure entire food webs, including protected habitats. The tractable system is also fully valid for being forced via its second equation by the oscillator of a partially migratory predator with a similar or delayed cycle. In further studies, incorporating a latency period to account for resident species interactions outside of partial migration cycles may prove more realistic. Therefore, future works could potentially unveil new complex regimes.

Ethical standard

The author has no relevant financial or non-financial interests to disclose.

Availability of data and material

The data that support the findings of this study are available from the corresponding author upon reasonable request.

Conflicts of interest

The author declares that there is no conflict of interest regarding the publication of this paper.

LITERATURE CITED

Alebraheem, J., 2021 Dynamics of a predator–prey model with the effect of oscillation of immigration of the prey. Diversity **13**: 23.

Alebraheem, J., T. Q. Ibrahim, G. E. Arif, A. A. Hamdi, O. Bazighifan, *et al.*, 2024 The stabilizing effect of small prey immigration on competitive predator-prey dynamics. Mathematical and Computer Modelling of Dynamical Systems **30**: 605–625.

Alerstam, T., M. Rosén, J. Bäckman, P. G. P. Ericson, and O. Hellgren, 2007 Flight speeds among bird species: Allometric and phylogenetic effects. PLoS Biology **5**: e197.

Ashwin, P., C. Perryman, and S. Wieczorek, 2017 Parameter shifts for nonautonomous systems in low dimension: Bifurcation- and rate-induced tipping. Nonlinearity **30**: 2185.

Berg, J. E., D. R. Eacker, M. Hebblewhite, and E. H. Merrill, 2023 Summer elk calf survival in a partially migratory population. Journal of Wildlife Management **87**: e22330.

Briedis, M., S. Hahn, M. Krist, and P. Adamík, 2018 Finish with a sprint: Evidence for time-selected last leg of migration in a long-distance migratory songbird. Ecology and Evolution **8**: 6899–6908.

Brodersen, J., B. B. Chapman, A. Nilsson, C. Skov, L.-A. Hansson, *et al.*, 2014 Fixed and flexible: Coexistence of obligate and facultative migratory strategies in a freshwater fish. PLoS ONE **9**: e90294.

Carpenter, S. R. *et al.*, 2011 Early warnings of regime shifts: A whole-ecosystem experiment. Science **332**: 1079–1082.

Chapman, B. B., C. Brönmark, J.- Nilsson, and L.-A. Hansson, 2011 Partial migration: An introduction. Oikos **120**: 1761–1763.

Dakos, V., S. R. Carpenter, E. H. van Nes, and M. Scheffer, 2015 Resilience indicators: Prospects and limitations for early warnings of regime shifts. Philosophical Transactions of the Royal Society B **370**: 20130263.

De Leenheer, P., A. Mohapatra, H. A. Ohms, D. A. Lytle, and J. M. Cushing, 2017 The puzzle of partial migration: Adaptive dynamics and evolutionary game theory perspectives. Journal of Theoretical Biology **412**: 172–185.

Doherty, J., J. Kutzbach, D. Foley, D. Pollard, *et al.*, 2000 Resilience stability of ecological systems. Climate Dynamics **16**: 561–573.

Elgin, C., 2004 True enough. Philosophical Issues **14**: 113–131, p.14.

Evers, K., D. Borsboom, E. I. Fried, F. Hasselman, and L. Waldorp, 2024 Early warning signals of complex critical transitions in deterministic dynamics. Nonlinear Dynamics **112**: 19071–19094.

Gottlieb, M. A. and R. Pfeiffer, 2013 The harmonic oscillator. https://www.feynmanlectures.caltech.edu/I_21.html, California Institute of Technology.

Guttal, V. and C. Jayaprakash, 2008 Changing skewness: An early warning signal of regime shifts in ecosystems. Ecology Letters **11**: 450–460.

Hansen, J. H., C. Skov, H. Baktoft, C. Brönmark, B. B. Chapman, *et al.*, 2019 Ecological consequences of animal migration: Prey partial migration affects predator ecology and prey communities. Ecosystems **22**: 1043–1056.

Hanski, I., 1999 *Metapopulation ecology*. Oxford University Press.

Holling, C. S., 1973 Resilience and stability of ecological systems. Annual Review of Ecology and Systematics **4**: 1–25.

Holt, R. D., 1985 Population dynamics in two-patch environments: Some anomalous consequences of an optimal habitat distribution. Theoretical Population Biology **28**: 181–208.

Kaitala, A., V. Kaitala, and P. Lundberg, 1993 A theory of partial migration. The American Naturalist **142**: 59–81.

Kangalgil, F. and S. Isik, 2022 Effect of immigration in a predator-prey system: Stability, bifurcation and chaos. AIMS Mathematics

7: 14354–14375.

Levins, R., 1969 Some demographic and genetic consequences of environmental heterogeneity for biological control. American Entomologist **15**: 237–240.

Lotka, A. J., 1925 *Elements of physical biology*. Williams & Wilkins.

Lundberg, P., 2013 On the evolutionary stability of partial migration. Journal of Theoretical Biology **321**: 36–39.

Nazarimehr, F., S. Jafari, S. M. Reza, S. M. R. H. Golpayegani, and J. C. Sprott, 2017 Can lyapunov exponent predict critical transitions in biological systems? Nonlinear Dynamics **88**: 1493–1500.

Nussbaumer, R., S. Bauer, L. Benoit, G. Mariethoz, F. Liechti, *et al.*, 2021 Quantifying year-round nocturnal bird migration with a fluid dynamics model. Journal of the Royal Society Interface **18**: 20210194.

Nussbaumer, R., B. Schmid, S. Bauer, and F. Liechti, 2022 Favorable winds speed up bird migration in spring but not in autumn. Ecology and Evolution **12**: e9146.

Peller, T., F. Guichard, and F. Altermatt, 2022 The significance of partial migration for food web and ecosystem dynamics. Ecology Letters **26**: 3–22.

Peterson, G., C. R. Allen, and C. S. Holling, 1998 Ecological resilience, biodiversity, and scale. Ecosystems **1**: 6–18.

Pulliam, H. R., 1988 Sources, sinks and population regulation. The American Naturalist **132**: 652–661, p. 652.

Scheffer, M., J. Bascompte, W. A. Brock, *et al.*, 2009 Early-warning signals for critical transitions. Nature **461**: 53–59.

Scheffer, M., S. Carpenter, J. A. Foley, C. Folke, and B. Walker, 2001 Catastrophic shifts in ecosystems. Nature **413**: 591–596.

Skov, C., B. B. Chapman, H. Baktoft, J. Brodersen, C. Brönmark, *et al.*, 2013 Migration confers survival benefits against avian predators for partially migratory freshwater fish. Biology Letters **9**: 20121178.

Smirnov, L. A. and A. Pikovsky, 2024 Dynamics of oscillator populations globally coupled with distributed phase shifts. Physical Review Letters **132**: 107401.

Tahara, T., M. K. A. Gavina, T. Kawano, J. M. Tubay, *et al.*, 2018 Asymptotic stability of a modified lotka-volterra model with small immigrations. Scientific Reports **8**: 7029.

Taylor, C. M. and R. J. Hall, 2012 Metapopulation models for seasonally migratory animals. Biology Letters **8**: 477–480.

Vandermeer, J., 2006 Oscillating populations and biodiversity maintenance. BioScience **56**: 967–975.

Vasseur, D. A. and J. W. Fox, 2009 Phase-locking and environmental fluctuations generate synchrony in a predator–prey community. Nature **460**: 1007–1010.

Vergara, P., J. I. Aguirre, and M. Fernandez-Cruz, 2007 Arrival date, age and breeding success in white stork ciconia ciconia. Journal of Avian Biology **38**: 573–579.

Volterra, V., 1926 Fluctuations in the abundance of a species considered mathematically. Nature **118**: 558–560.

Volterra, V., 1931 Variations and fluctuations of the number of individuals in animal species living together. In *Animal Ecology*, edited by R. N. Chapman, p. 7, McGraw-Hill, 6th edition.

Winfree, A. T., 1967 Biological rhythms and the behavior of populations of coupled oscillators. Journal of Theoretical Biology **16**: 15–42.

Zúñiga, D., Y. Gager, H. Kokko, A. M. Fudickar, A. Schmidt, *et al.*, 2017 Migration confers winter survival benefits in a partially migratory songbird. eLife **6**: e28123.

How to cite this article: Bouali, S. Partial Prey Migration as a Non-autonomous Harmonic Oscillator: Chaos-Order Transitions in a Forced Classical Lotka-Volterra Model. *Chaos and Fractals*, 2(2), 50-58, 2025.